An adaptive coupling method of state-based peridynamics theory and finite element method for modeling progressive failure process in cohesive materials

Yue Tong, Wanqing Shen, Jian-Fu Shao

Version of Record: https://www.sciencedirect.com/science/article/pii/S0045782520304333
Manuscript_d2d99898722944c9fec10a0a6c3c1af5

An adaptive coupling method of state-based peridynamics theory and finite element method for modeling progressive failure process in cohesive materials

Yue Tong[a,b], Wan-Qing Shen[a,b], Jian-Fu Shao[a,b,*]

[a] *Key Laboratory of Ministry of Education on Safe Mining of Deep Metal Mines, College of Resources and Civil Engineering, Northeastern University, Shenyang, 110819, China*
[b] *Univ. Lille, CNRS, Centrale Lille, UMR 9013 - LaMcube - Laboratoire de Mécanique, Multiphysique, Multi-échelle, F-59000 Lille, France*

Abstract

In this study, an adaptive coupling method is proposed for the combination of the state-based peridynamics theory (PD) and the classical finite element method (FEM). The non-local PD theory is used for dealing with localized cracking process while the FEM is adopted for modeling elastic (or plastic) problems without localization. The evolving boundary between cracking domain and the elastic or plastic domain without localization is taken into account. A new bond damage model is implemented into the ordinary state-based PD theory, by considering the progressive degradation of bond strength and residual strength. The proposed coupling method and bond damage model are implemented in MATLAB framework. The accuracy of the FEM-PD coupling method is verified by the analytical solutions in elastic cases. The efficiency of the new bond damage model implemented in the adaptive FEM-PD coupling method for modeling the progressive failure process in cohesive materials is clearly validated through a series of representative laboratory tests on concrete structures.

Keywords: State-based peridynamics theory, Finite element method, Adaptive coupling, Crack propagation, Progressive failure, Cohesive materials

1. Introduction

Failure in cohesive geological and cement-based materials is relevant to the transition from diffuse micro-cracking to localized macro-fracturing (Bažant, 1976, Shao and Rudnicki, 2000, Zhao et al., 2018). The macroscopic failure is generally a progressive process due to the internal cohesion of those materials (Hillerborg et al., 1976, Rots, 1988, Moës and Belytschko, 2002). Unlike propagation modeling of a single existing crack, modelling of the progressive failure from the onset, coalescence and localization of multiple cracks is still open issue.

Considerable efforts have been provided and different kinds of numerical methods have been developed during recent decades. Not exhaustively but representatively, some of them are here mentioned. The enriched finite element method (EFEM) (Oliver, 1996) with elementary enrichments and the eXtended finite

*Corresponding author: jian-fu.shao@polytech-lille.fr

element method (XFEM) (Moës et al., 1999, Stolarska et al., 2001) with node enrichments have been widely used for dealing with cracking problems with strong discontinuities, even with hydromechanical coupling (Zeng et al., 2018, 2019). Some comparative studies of different kinds of numerical methods can be found in (Jirásek, 2000, Dias-da Costa et al., 2010). But in those previous studies, the choice of specific enrichment functions and crack propagation criteria was a key issue and not an easy task (Wu et al., 2018, 2019). Further, the ability of those methods in dealing with crack coalescence and branching as well as multiple cracks propagation is still not fully demonstrated. More recently, the phase-field methods have been developed by approximating the sharp crack topology by the regularised one (Miehe et al., 2010). This class of methods attracted more and more attention due to their efficiency for describing the transition from diffuse damage to localized cracking. However, the development of the real crack is represented by the localized damage band which requires an extra scale length parameter to characterize its width (Molnár and Gravouil, 2017, Wang et al., 2019).

On the other hand, the *peridynamics* (PD) theory has been developed as an extension of classical continuum mechanics framework (Silling, 2000). Instead of solving partially derivative equations, which is particularly delicate with the presence of crack singularities, integral motion equations are solved in PD theory. Therefore, this theory is particularly efficient for dealing with cracking problems (Madenci and Oterkus, 2014). The cracking process of continuum is directly related to the damage of internal material bonds or links. Therefore, the initiation and propagation of cracks can be naturally described without introducing any extra crack propagation criteria or crack-tracking method. In terms of interactions between internal material points, two different formulations of the PD theory are proposed. The bond-based PD theory was first formulated by only considering pair-wise interactions between two neighboring points (Silling, 2000). More recently, some improvements have been proposed in the bond-based PD theory by introducing rotation effect in order to avoid the restriction of Poisson's ratio (Zhu and Ni, 2017, Ni et al., 2019). In order to describe more complex deformation mechanisms, the state-based PD theory has further been developed (Silling et al., 2007). The motion of each material point depends on the interactions with all other points inside a limited surrounding zone (Silling et al., 2007). The classical concepts of local stress and strain tensors are generalized to the non-local force and deformation states. The constitutive equations are thus described by the relations between such states. In addition, the state-based PD theory is able to conveniently describe distortional and volumetric deformations other than the single volumetric deformation in the bond-based one (Silling and Lehoucq, 2010, Madenci and Oterkus, 2014). Thus, the state-based PD is suitable for modeling the deformation and failure of geological materials, for which the shearing induced volumetric dilatancy is an important feature. However, owing to the non-local formulations, the numerical methods based on the PD theories are computationally time-consuming. In view of studying large scale boundary values problems, it is generally convenient to combine the PD theories in cracking zones with the finite element method (FEM) in elastic or plastic zones. A number of works have been reported on the combination of bond-based PD theory and FEM (Macek and Silling, 2007, Shojaei et al., 2016, Zaccariotto et al., 2018). More recently, the state-based PD theory was also been combined with the FEM framework (Madenci et al., 2018, Bie et al., 2018).

In terms of description of bond damage, different kinds of criteria have been formulated. For instance, a critical bond stretch criterion for the prototype micro-elastic brittle (PMB) material was first proposed and implemented in the bond-based PD theory in (Silling and Askari, 2005). This criterion has been widely applied to simulate brittle fracture problems (Javili et al., 2018, Diehl et al., 2019). Some improvements have been obtained by using a trilinear bond model (Yang et al., 2018). Similar critical bond stretch criteria have also been introduced into the state-based PD theory for brittle materials (Madenci and Oterkus, 2014, Zhang and Qiao, 2018). However, all those brittle models are not able to correctly describe the progressive failure process in cohesive materials such as concrete (Petersson, 1981, Hoover and Bažant, 2014). In particular, the progressive softening behavior on the post-peak regime is badly reproduced.

More recently, a new bond continuum damage model has been formulated in the framework of the bond-based PD theory (Tong et al., 2020). In order to overcome the limitations of the bond-based PD theory, the bond continuum damage model is here extended to the state-based PD theory, in order to better modeling the progressive failure process in cohesive geological materials, especially for the compressive shearing conditions. Further, an adaptive switching strategy is also developed for coupling with the standard finite element method. The capability of the proposed bond damage model as well as the coupling strategy will be verified through three representative laboratory tests.

This paper is organized as follows. The general framework of the ordinary state-based PD theory is first presented in section 2. In section 3, a new bond continuum damage model for cohesive materials is introduced into the ordinary state-based PD theory. In section 4, an adaptively strategy for coupling the PD theory and finite element method is established. In section 5, the effectiveness of the coupling method considering the damage or not is verified.

2. The ordinary state-based PD theory

The state-based PD theory can be seen as a generalized framework for the classical solid mechanics (Silling et al., 2007, Silling and Lehoucq, 2010). The kernel is the use of the *state* concept for mapping deformation at a material point by including the information of all internal bonds linking to other material points within its horizon zone. As shown in Figure 1, every material point $\boldsymbol{x}$ interacts directly with other material points $\boldsymbol{x'}$ within its horizon $H_{\boldsymbol{x}}$ determined by the prescribed horizon radius δ. Due to the external loading, the solid body deforms. Accordingly, the material points $\boldsymbol{x}$, $\boldsymbol{x'}$ at the initial configuration are moved to $\boldsymbol{y}$, $\boldsymbol{y'}$ in the deformed configuration. Now the vector $\underline{\boldsymbol{X}}$ is defined as the reference vector state mapping the initial position of one bond as:

$$\underline{\boldsymbol{X}}\langle \boldsymbol{x'} - \boldsymbol{x} \rangle = \boldsymbol{x'} - \boldsymbol{x} \tag{1}$$

and $\underline{\boldsymbol{Y}}$ as the deformation vector state mapping the bond into its deformed image as:

$$\underline{\boldsymbol{Y}}[\boldsymbol{x}, t]\langle \boldsymbol{x'} - \boldsymbol{x} \rangle = \boldsymbol{y}(\boldsymbol{x'}, t) - \boldsymbol{y}(\boldsymbol{x}, t) \tag{2}$$

In these definitions $\boldsymbol{y}(\boldsymbol{x}, t) = \boldsymbol{x} + \boldsymbol{u}(\boldsymbol{x}, t)$, $\boldsymbol{y}(\boldsymbol{x'}, t) = \boldsymbol{x} + \boldsymbol{u}(\boldsymbol{x'}, t)$, $\boldsymbol{u}(\boldsymbol{x}, t)$ and $\boldsymbol{u}(\boldsymbol{x'}, t)$ are the displacement vectors associated to $\boldsymbol{x}$ and $\boldsymbol{x'}$ respectively. Besides, let $\underline{\boldsymbol{T}}$ define the force density vector state. The force

vector states related to $\boldsymbol{x}$ and $\boldsymbol{x'}$ are respectively $\underline{\boldsymbol{T}}[\boldsymbol{x}, t]$ and $\underline{\boldsymbol{T}}[\boldsymbol{x'}, t]$. If the force state $\underline{\boldsymbol{T}}$ is aligned with the deformation state $\underline{\boldsymbol{Y}}$, the PD theory is named as the *ordinary* state-based. Otherwise, it is called as the *non-ordinary* state-based PD theory. In this paper, the *ordinary* state-based PD theory is applied. In this case, the motion equation of a material point is defined as: as(Silling et al., 2007):

$$\boldsymbol{\rho}(\boldsymbol{x})\ddot{\boldsymbol{u}}(\boldsymbol{x}, t) = \int_{H_x} \{\underline{\boldsymbol{T}}[\boldsymbol{x}, t]\langle \boldsymbol{x'} - \boldsymbol{x}\rangle - \underline{\boldsymbol{T}}[\boldsymbol{x'}, t]\langle \boldsymbol{x} - \boldsymbol{x'}\rangle\} dV_{\boldsymbol{x'}} + \boldsymbol{b}(\boldsymbol{x}, t) \tag{3}$$

where $\boldsymbol{\rho}(\boldsymbol{x})$ is the mass density, $V_{\boldsymbol{x'}}$ the volume associated with the material point $\boldsymbol{x'}$, and $\boldsymbol{b}(\boldsymbol{x}, t)$ the external body force density.

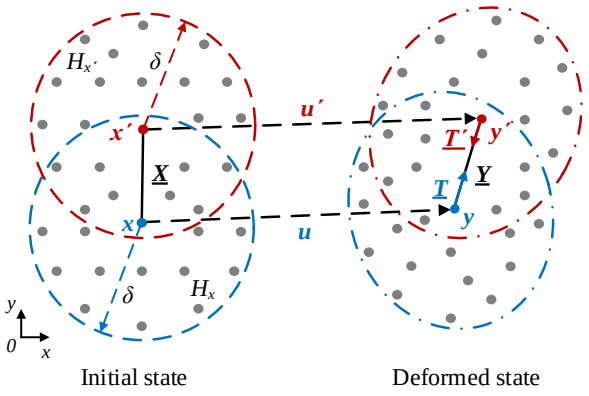

Figure 1: Illustration of the ordinary stated-based peridynamics theory

For numerical implementation, the integral formulation (3) is approximation by the discrete for a given PD material point $\boldsymbol{x_k}$:

$$\boldsymbol{\rho}(\boldsymbol{x_k})\ddot{\boldsymbol{u}}(\boldsymbol{x_k}, t) = \sum_{j=1}^{N} (\underline{\boldsymbol{T}}\langle \boldsymbol{x_j} - \boldsymbol{x_k}\rangle - \underline{\boldsymbol{T}}\langle \boldsymbol{x_k} - \boldsymbol{x_j}\rangle) V_j + \boldsymbol{b}(\boldsymbol{x_k}, t) \tag{4}$$

in which N is the number of material points ($\boldsymbol{x_j}$) within the horizon of $\boldsymbol{x_k}$, V_j is the volume of $\boldsymbol{x_j}$. For the case of static or quasi static problems, (4) is simplified to:

$$\boldsymbol{0} = \sum_{j=1}^{N} (\underline{\boldsymbol{T}}\langle \boldsymbol{x_j} - \boldsymbol{x_k}\rangle - \underline{\boldsymbol{T}}\langle \boldsymbol{x_k} - \boldsymbol{x_j}\rangle) V_j + \boldsymbol{b}(\boldsymbol{x_k}) \tag{5}$$

As in the classical continuum mechanics, the force state can be obtained from the derivation of an energy functional $W(\boldsymbol{x})$ with respect to the deformation state (Madenci and Oterkus, 2014). For instance, the force states for the material points $\boldsymbol{x_k}$ and $\boldsymbol{x_j}$ can be expressed as follows:

$$\underline{\boldsymbol{T}}\langle \boldsymbol{x_j} - \boldsymbol{x_k}\rangle = \frac{1}{V_j} \frac{\partial W(\boldsymbol{x_k})}{\partial(|\boldsymbol{y_j} - \boldsymbol{y_k}|)} \frac{\boldsymbol{y_j} - \boldsymbol{y_k}}{|\boldsymbol{y_j} - \boldsymbol{y_k}|} \tag{6}$$

and

$$\underline{\boldsymbol{T}}\langle \boldsymbol{x_k} - \boldsymbol{x_j}\rangle = \frac{1}{V_k} \frac{\partial W(\boldsymbol{x_j})}{\partial(|\boldsymbol{y_k} - \boldsymbol{y_j}|)} \frac{\boldsymbol{y_k} - \boldsymbol{y_j}}{|\boldsymbol{y_k} - \boldsymbol{y_j}|} \tag{7}$$

For isotropic and elastic materials, the generalized form of the strain energy density function $W(\boldsymbol{x})$ at any PD material point $\boldsymbol{x_k}$ is defined as:

$$W(\boldsymbol{x_k}) = a\theta(\boldsymbol{x_k})^2 + b\sum_{j=1}^{N}\omega_{kj}(|\boldsymbol{y_j}-\boldsymbol{y_k}|-|\boldsymbol{x_j}-\boldsymbol{x_k}|)^2 V_j \tag{8}$$

The term $\theta(\boldsymbol{x_k})$ is related to volume dilatation and calculated by:

$$\theta(\boldsymbol{x_k}) = d\sum_{j=1}^{N}\omega_{kj}(|\boldsymbol{y_j}-\boldsymbol{y_k}|-|\boldsymbol{x_j}-\boldsymbol{x_k}|)\frac{\boldsymbol{y_j}-\boldsymbol{y_k}}{|\boldsymbol{y_j}-\boldsymbol{y_k}|}\frac{\boldsymbol{x_j}-\boldsymbol{x_k}}{|\boldsymbol{x_j}-\boldsymbol{x_k}|}V_j \tag{9}$$

In these expressions, a, b and d are three PD parameters which are related to the macroscopic elastic constants of materials and the PD horizon radius. ω_{kj} is a non-dimensional influence function which reflects the degree of non-locality between material points so that the interaction between points decreases as the distance increases (Madenci et al., 2016).

With the assumption of small deformation, the following simplifying relations can be adopted:

$$|\boldsymbol{u}(\boldsymbol{x_j})-\boldsymbol{u}(\boldsymbol{x_k})| << |\boldsymbol{x_j}-\boldsymbol{x_k}| \tag{10}$$

$$\frac{\boldsymbol{y_j}-\boldsymbol{y_k}}{|\boldsymbol{y_j}-\boldsymbol{y_k}|}\frac{\boldsymbol{x_j}-\boldsymbol{x_k}}{|\boldsymbol{x_j}-\boldsymbol{x_k}|} \approx 1 \tag{11}$$

Further, by defining the influence function ω_{kj} as:

$$\omega_{kj} = \frac{\delta}{|\boldsymbol{x_j}-\boldsymbol{x_k}|} \tag{12}$$

the force vector states in (6) and (7) can be rewtitten as:

$$\underline{\boldsymbol{T}}\langle\boldsymbol{x_j}-\boldsymbol{x_k}\rangle = \left(\frac{2ad^2\delta^2}{|\boldsymbol{x_j}-\boldsymbol{x_k}|}\sum_{m=1}^{N}\frac{|\boldsymbol{y_m}-\boldsymbol{y_k}|-|\boldsymbol{x_m}-\boldsymbol{x_k}|}{|\boldsymbol{x_m}-\boldsymbol{x_k}|}V_m + 2b\delta\frac{|\boldsymbol{y_j}-\boldsymbol{y_k}|-|\boldsymbol{x_j}-\boldsymbol{x_k}|}{|\boldsymbol{x_j}-\boldsymbol{x_k}|}\right)\frac{\boldsymbol{x_j}-\boldsymbol{x_k}}{|\boldsymbol{x_j}-\boldsymbol{x_k}|} \tag{13}$$

and

$$\underline{\boldsymbol{T}}\langle\boldsymbol{x_k}-\boldsymbol{x_j}\rangle = \left(\frac{2ad^2\delta^2}{|\boldsymbol{x_k}-\boldsymbol{x_j}|}\sum_{n=1}^{N}\frac{|\boldsymbol{y_n}-\boldsymbol{y_j}|-|\boldsymbol{x_n}-\boldsymbol{x_j}|}{|\boldsymbol{x_n}-\boldsymbol{x_j}|}V_n + 2b\delta\frac{|\boldsymbol{y_k}-\boldsymbol{y_j}|-|\boldsymbol{x_k}-\boldsymbol{x_j}|}{|\boldsymbol{x_k}-\boldsymbol{x_j}|}\right)\frac{\boldsymbol{x_k}-\boldsymbol{x_j}}{|\boldsymbol{x_k}-\boldsymbol{x_j}|} \tag{14}$$

where $\boldsymbol{x_m}$ and $\boldsymbol{x_n}$ denote the material points within the respective horizon of $\boldsymbol{x_k}$ and $\boldsymbol{x_j}$. Now by using the equivalence condition between the classical continuum mechanics and PD theory of the elastic strain energy respectively for the shear strain part $W(\boldsymbol{x})$ and the volumetric strain part $\theta(\boldsymbol{x})$, the PD parameters a, b and d can be identified (Madenci and Oterkus, 2014):

$$\begin{cases} a = \dfrac{1}{2}(k-\dfrac{5}{3}\mu), b = \dfrac{15\mu}{2\pi\delta^5}, d = \dfrac{9}{4\pi\delta^4}, & \text{3D} \\ a = \dfrac{1}{2}(k-2\mu), b = \dfrac{6\mu}{\pi h\delta^4}, d = \dfrac{2}{\pi h\delta^3}, & \text{2D} \\ a = 0, b = \dfrac{E}{2A\delta^3}, d = \dfrac{1}{2A\delta^2}, & \text{1D} \end{cases} . \tag{15}$$

where k, μ and E are the macroscopic bulk modulus, the shear modulus and the Young's modulus, h is the thickness for 2D geometry, A is the cross sectional area for 1D geometry. And k and μ are expressed of Young's modulus E and Poisson's ratio ν by:

$$k = \begin{cases} \dfrac{E}{3(1-2\nu)}, & \text{3D} \\ \dfrac{E}{2(1-\nu)}, & \text{plane stress} \\ \dfrac{E}{2(1+\nu)(1-2\nu)}, & \text{plane strain} \end{cases} \quad , \quad \mu = \frac{E}{2(1+\nu)} \tag{16}$$

As in the bond-based PD theory (Foster et al., 2011, Zhang and Qiao, 2018), the stretch (deformation) of the *bond* linking a pair of two points $\boldsymbol{x_k}$ and $\boldsymbol{x_j}$ is denoted as s_{kj} and calculated by:

$$s_{kj} = \frac{|\boldsymbol{y_j} - \boldsymbol{y_k}| - |\boldsymbol{x_j} - \boldsymbol{x_k}|}{|\boldsymbol{x_j} - \boldsymbol{x_k}|} \tag{17}$$

Substituting (17) for (13) and (14), the force states are explicitly expressed as functions of the bond stretches:

$$\underline{\boldsymbol{T}}\langle \boldsymbol{x_j} - \boldsymbol{x_k} \rangle = \left(\frac{2ad^2\delta^2}{|\boldsymbol{x_j} - \boldsymbol{x_k}|} \sum_{m=1}^{N} s_{km} V_m + 2b\delta s_{kj}\right) \frac{\boldsymbol{x_j} - \boldsymbol{x_k}}{|\boldsymbol{x_j} - \boldsymbol{x_k}|} \tag{18}$$

and

$$\underline{\boldsymbol{T}}\langle \boldsymbol{x_k} - \boldsymbol{x_j} \rangle = \left(\frac{2ad^2\delta^2}{|\boldsymbol{x_k} - \boldsymbol{x_j}|} \sum_{n=1}^{N} s_{jn} V_n + 2b\delta s_{jk}\right) \frac{\boldsymbol{x_k} - \boldsymbol{x_j}}{|\boldsymbol{x_k} - \boldsymbol{x_j}|} \tag{19}$$

The interaction between two materials points can now be defined by a generalized pairwise force density function as follows:

$$\tilde{\boldsymbol{f}}\langle \boldsymbol{x_j} - \boldsymbol{x_k} \rangle = \underline{\boldsymbol{T}}\langle \boldsymbol{x_j} - \boldsymbol{x_k} \rangle - \underline{\boldsymbol{T}}\langle \boldsymbol{x_k} - \boldsymbol{x_j} \rangle \tag{20}$$

Substituting (18) and (19) for (20), one gets:

$$\tilde{\boldsymbol{f}}\langle \boldsymbol{x_j} - \boldsymbol{x_k} \rangle = \left(4b\delta s_{kj} + \frac{2ad^2\delta^2}{|\boldsymbol{x_j} - \boldsymbol{x_k}|} \left(\sum_{m=1}^{N} s_{km} V_m + \sum_{n=1}^{N} s_{jn} V_n\right)\right) \frac{\boldsymbol{x_j} - \boldsymbol{x_k}}{|\boldsymbol{x_j} - \boldsymbol{x_k}|} \tag{21}$$

Like the that defined in the bond-based PD theory, the generalized pairwise force density function is also a function of stretches of paired points. However, as a fundamental difference, it not only depends on the own stretches of the paired points but also on the stretches associated with the points within their horizons.

Based on the above relation between the pairwise force and stretch, it appears convenient to introduce a local damage criterion as a function of the *bond stretch* to describe progressive failure of materials. That means that when the stretch of a bond reaches a critical value, the bond is progressively broken and the corresponding pairwise force decreases. The effect of bond damage on the bond force is here described by introducing a history dependent scalar function ζ_{kj}, which represents the status of the invented bond

connecting $\boldsymbol{x_k}$ and $\boldsymbol{x_j}$. Consequently, the generalized pairwise force density function is updated by taking into account the bond damage:

$$\tilde{\boldsymbol{f}}\langle \boldsymbol{x_j} - \boldsymbol{x_k} \rangle = \zeta_{kj} \left(4b\delta s_{kj} + \frac{2ad^2\delta^2}{|\boldsymbol{x_j} - \boldsymbol{x_k}|} \left(\sum_{m=1}^{N} \zeta_{km} s_{km} V_m + \sum_{n=1}^{N} \zeta_{jn} s_{jn} V_n \right) \right) \frac{\boldsymbol{x_j} - \boldsymbol{x_k}}{|\boldsymbol{x_j} - \boldsymbol{x_k}|} \tag{22}$$

In the basic model for prototype micro-elastic brittle (PMB) material (Silling and Askari, 2005, Madenci and Oterkus, 2014), the status function ζ_{kj} is defined as follows:

$$\zeta_{kj} = \begin{cases} 1, & s_{kj} < s_c \\ \\ 0, & \text{otherwise} \end{cases} . \tag{23}$$

where s_c is the critical bond stretch. According to this model, the interaction force between the paired points increases linearly with the stretch and drops abruptly as the stretch reaches the critical value, as shown in Figure 2a. The value of s_c can be determined by considering that the work required to break all bonds across a newly created crack surface is equivalent to the macroscopic critical energy release rate G_c, one gets:

$$s_c = \begin{cases} \sqrt{\dfrac{G_c}{\left((3\mu + (\frac{3}{4})^4 (k - \frac{5\mu}{3}) \right) \delta}}, & \text{3D} \\ \\ \sqrt{\dfrac{G_c}{\left(\frac{6}{\pi}\mu + \frac{16}{9\pi^2}(k - 2\mu) \right) \delta}}, & \text{2D} \end{cases} . \tag{24}$$

With a fixed value of Poisson's ratio ν=1/4 for 3D cases or 2D plane strain cases and ν=1/3 for 2D plane stress cases, the terms $(k - \frac{5\mu}{3})$ and $(k - 2\mu)$ in (24) vanish and one gets the critical bond stretch value used in the bond-based PD theory.

Finally, the macroscopic damage state at any PD point x_k is quantified by the scalar variable $\varphi(x_k) \in [0, 1]$, which defines the ratio of the number of broken bonds to the total number of bonds:

$$\varphi(x_k) = 1 - \sum_{j=1}^{N} \zeta_{kj} / N \tag{25}$$

3. Bond damage model for cohesive materials

The basic elastic brittle model illustrated in Figure 2a has widely used in modeling brittle failure in elastic materials generally subjected to tensile stresses (Javili et al., 2018, Diehl et al., 2019). However, as mentioned above, the failure of cohesive materials under compressive stresses is a progressive process through the initiation and propagation of cracks in cohesive zones (Planas et al., 1993, Li and Bažant, 1994, Zi and Bažant, 2003, Hoover and Bažant, 2014). At the macroscopic scale, one obtains a smooth decrease of loading capacity in the post-peak regime (Petersson, 1981, Reinhardt et al., 1986, Bažant, 2002). Obviously, the basic elastic brittle model is not able to correctly describe such failure process. Therefore, a new bond

damage model is here proposed in the framework of the state-based PD theory. To this end, the bond status function for any paired points $\boldsymbol{x_k}$ and $\boldsymbol{x_j}$ is first modified as follows:

$$\zeta_{kj} = \frac{\tilde{\boldsymbol{f}}\langle \boldsymbol{x_j} - \boldsymbol{x_k} \rangle}{\tilde{\boldsymbol{f}}_{max}\langle \boldsymbol{x_j} - \boldsymbol{x_k} \rangle} \tag{26}$$

where $\tilde{\boldsymbol{f}}_{max}\langle \boldsymbol{x_j} - \boldsymbol{x_k} \rangle$ denotes the peak value of the bond force density while the bond stretch reaches the elastic limit. Compared with that defined in the bond-based PD theory, the new status function directly reflects the current degradation state of the bond force.

Furthermore, the status function is here expressed as a continuous function of the bond stretch. According to the result obtained in a concrete beam bending test (Rots, 1988), the global load-deflection response can be described by using an exponential form of the stress-crack opening relation. Inspired by this results, the exponential law has widely used in modeling tensile softening in concrete materials and structures (Bazant and Li, 1997, Winkler et al., 2004, Grassl and Jirásek, 2006, Unger et al., 2007, **?**, Wu, 2017, Le et al., 2018). Based on those previous studies, an exponential damage evolution function is here introduced to describe the local mechanical behavior of bonds for cohesive materials. The new status function is then defined as:

$$\zeta_{kj} = \begin{cases} 1, & s \le s_0 \\ e^{-k_1 \frac{s - s_0}{s_0}} + k_2 \frac{s - s_0}{s}, & s > s_0 \end{cases} . \tag{27}$$

where s_0 denotes the elastic limit stretch, defining the damage initiation of bond. The parameter k_1 controls the reduction rate of bond force as a function of bond stretch. And the parameter k_2 gives the residual bond force. As a basic difference with (23), the new status function in (27) evolves continuously from 0 to 1, reflecting the progressive damage of bond. With the new bond damage model proposed in (26), (23) and (27), the evolutions of bond force and status function are presented in Figure 2b.

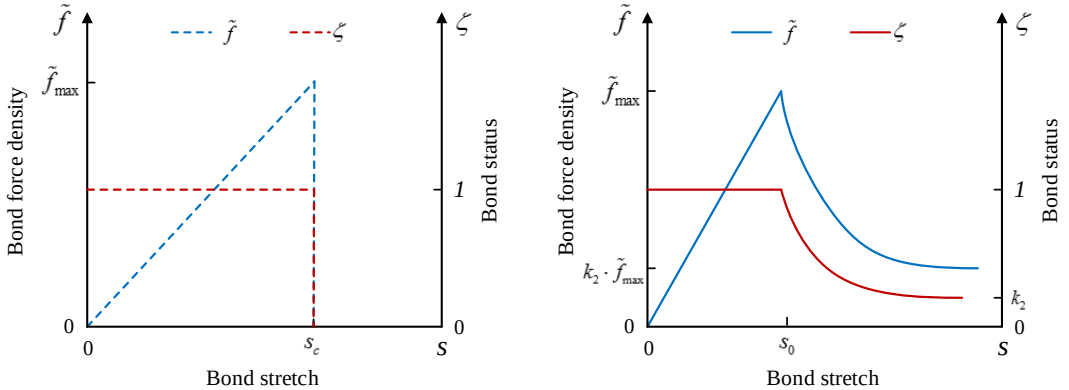

(a) PMB material model

(b) Cohesive brittle material model

Figure 2: Evolutions of bond force and status function respectively in the PMB model (a) and new cohesive bond damage model (b)

The bond stretch elastic limit s_0, the bond force reduction parameter k_1 and the residual bond force parameter k_2 are now determined to completely calibrate the new bond damage model for the state-based PD theory. Similarly to the bond-based theory, the value of s_0 is also related to the macroscopic critical fracture energy G_c. As depicted in Figure 3, the formation of a new crack surface requires the breakage of all bonds between the material points $\boldsymbol{x_{k^+}}$ (above the crack surface) and $\boldsymbol{x_{j^-}}$ (below the crack surface). Let K^- denote the number of material points within the horizon of $\boldsymbol{x_{k^+}}$ below the crack surface and intersecting with the crack surface. And let J^+ represent the number of material points within the horizon of $\boldsymbol{x_{j^-}}$ above the crack surface and intersecting with the crack surface. By making use of (22) and (27), the critical energy density needed to eliminate the interaction force between $\boldsymbol{x_{k^+}}$ and $\boldsymbol{x_{j^-}}$ is given by:

$$\begin{aligned} w &= \int_0^s \tilde{f}\xi ds \\ &= 4b\delta\xi s_0^2\left(\frac{1}{2}+\frac{1}{k_1}(1-e^{-k_1\frac{s-s_0}{s_0}})+k_2(\frac{s-s_0}{s_0}-ln\frac{s}{s_0})\right) \\ &+ 2ad^2\delta^2 s_0^2\left(\frac{1}{2}+\frac{1}{2k_1}(1-e^{-2k_1\frac{s-s_0}{s_0}})+\frac{2k_2}{k_1}(1-e^{-k_1\frac{s-s_0}{s_0}})+k_2^2(\frac{s^2-s_0^2}{ss_0}-2ln\frac{s}{s_0})\right)\left(\sum_{m=1}^{K^-}V_m+\sum_{n=1}^{J^+}V_n\right) \end{aligned} \tag{28}$$

in which $\xi = |\boldsymbol{x_{k^+}} - \boldsymbol{x_{j^-}}|$.

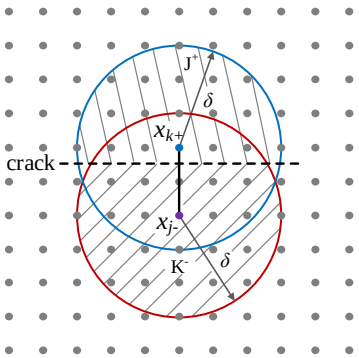

Figure 3: Sketch map of the interaction between pairwise points crossing a crack surface

The last term in the bracket of (28) represents the horizon volume of the bond and can be related to the horizon radius by:

$$\left(\sum_{m=1}^{K^-}V_m+\sum_{n=1}^{J^+}V_n\right)=\begin{cases}\dfrac{\pi\delta^3}{2}, & \text{3D case}\\[2ex] \dfrac{4h\delta^2}{3}, & \text{2D case}\end{cases}. \tag{29}$$

Subsequently, the sum of energy used to break all the bonds crossing the unit area of a new crack surface is

assumed to be equal to macroscopic fracture energy. Thus one gets for 3D cases:

$$\begin{aligned} G_c &= \int_0^{\delta}\int_0^{2\pi}\int_z^{\delta}\int_0^{cos^{-1}\frac{z}{\xi}} w\xi^2 sin\phi d\phi d\phi d\xi d\theta dz \\ &= \frac{2\pi b\delta^6}{5}s_0^2\left(1+\frac{2}{k_1}(1-e^{-k_1\frac{s-s_0}{s_0}})+2k_2(\frac{s-s_0}{s_0}-ln\frac{s}{s_0})\right) \\ &+ \frac{\pi^2 ad^2\delta^9}{8}s_0^2\left(1+\frac{1}{k_1}(1-e^{-2k_1\frac{s-s_0}{s_0}})+\frac{4k_2}{k_1}(1-e^{-k_1\frac{s-s_0}{s_0}})+2k_2^2(\frac{s^2-s_0^2}{ss_0}-2ln\frac{s}{s_0})\right) \end{aligned} \tag{30}$$

and for 2D cases:

$$\begin{aligned} G_c &= 2h\int_0^{\delta}\int_z^{\delta}\int_0^{cos^{-1}\frac{z}{\xi}} w\xi d\phi d\xi dz \\ &= bh\delta^5 s_0^2\left(1+\frac{2}{k_1}(1-e^{-k_1\frac{s-s_0}{s_0}})+2k_2(\frac{s-s_0}{s_0}-ln\frac{s}{s_0})\right) \\ &+ \frac{8ad^2h^2\delta^7}{9}s_0^2\left(1+\frac{1}{k_1}(1-e^{-2k_1\frac{s-s_0}{s_0}})+\frac{4k_2}{k_1}(1-e^{-k_1\frac{s-s_0}{s_0}})+2k_2^2(\frac{s^2-s_0^2}{ss_0}-2ln\frac{s}{s_0})\right) \end{aligned} \tag{31}$$

According to (30) and (31), the bond stretch elastic limit s_0 cannot be directly determined from G_c due to the unknown values of k_1 and k_2. Thus, some simplifications are here made. It is first assumed that the energy related to the residual bond force is a very small part in the total energy. This leads to set k_2 to 0. It is further considered that the bond failure occurs when s is significantly larger than s_0. Thus the values of $(1-e^{-k_1\frac{s-s_0}{s_0}})$ and $(1-e^{-2k_1\frac{s-s_0}{s_0}})$ are approximatively equal to 1. Based on these simplifications, the value of s_0 can be calculated by:

$$s_0 = \begin{cases} \sqrt{\dfrac{G_c}{\frac{2\pi b\delta^6}{5}(1+\frac{2}{k_1})+\frac{\pi^2 ad^2\delta^9}{8}(1+\frac{1}{k_1})}}, & \text{3D} \\ \sqrt{\dfrac{G_c}{bh\delta^5(1+\frac{2}{k_1})+\frac{8ad^2h^2\delta^7}{9}(1+\frac{1}{k_1})}}, & \text{2D} \end{cases} . \tag{32}$$

The above relations can be further simplified. To this end, the coefficients g_1 and g_2 are introduced as follows:

$$g_1 = \begin{cases} \dfrac{2\pi b\delta^6}{5}, & \text{3D} \\ bh\delta^5, & \text{2D} \end{cases}, \; g_2 = \begin{cases} \dfrac{\pi^2 ad^2\delta^9}{8}, & \text{3D} \\ \dfrac{8ad^2h^2\delta^7}{9}, & \text{2D} \end{cases} . \tag{33}$$

By taking the expressions of b and d from (15) and (16), the absolute value of the ratio $\frac{g_2}{g_1}$ is given by:

$$|\frac{g_2}{g_1}| = \begin{cases} |\frac{27(4\nu-1)}{256(1-2\nu)}|, & \text{3D} \\ |\frac{8(3\nu-1)}{27\pi(1-\nu)}|, & \text{plane stress} \\ |\frac{8(4\nu-1)}{27\pi(1-2\nu)}|, & \text{plane strain} \end{cases} . \tag{34}$$

It is seen that the value of $|\frac{g_2}{g_1}|$ depends on Poisson's ratio ν, as shown in Figure 4. One can see that the value of $|\frac{g_2}{g_1}|$ remains much smaller than unit for the range of ν from 0.15 to 0.35. Based on (9), that means that the energy caused by the distortional deformation (controlled by g_1) is the dominating part against the energy related to the volumetric deformation (controlled by g_2). Based on this fact, it is possible to take $(1 + \frac{1}{k_1}) \simeq (1 + \frac{2}{k_1})$. Accordingly, the value of s_0 can now be calculated by:

$$s_0 = \begin{cases} \sqrt{\dfrac{G_c}{(\frac{2\pi b\delta^6}{5} + \frac{\pi^2 a d^2 \delta^9}{8})(1 + \frac{2}{k_1})}}, & \text{3D} \\ \sqrt{\dfrac{G_c}{(bh\delta^5 + \frac{8ad^2h^2\delta^7}{9})(1 + \frac{2}{k_1})}}, & \text{2D} \end{cases} . \tag{35}$$

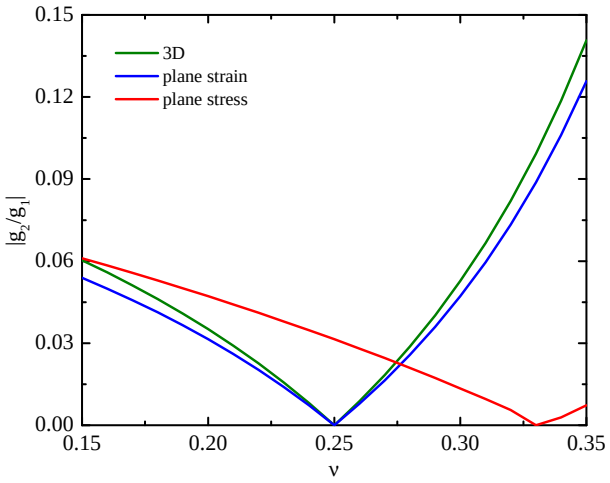

Figure 4: Variation of $|\frac{g_2}{g_1}|$ with ν

By replacing again the expressions of b and d, the elastic limit of bond stretch s_0 is expressed as a function of macroscopic elastic properties:

$$s_0 = \begin{cases} \sqrt{\dfrac{G_c}{\left((3\mu + (\frac{3}{4})^4(k - \frac{5\mu}{3})\right)(1 + \frac{2}{k_1})\delta}}, & \text{3D} \\ \sqrt{\dfrac{G_c}{\left(\frac{6}{\pi}\mu + \frac{16}{9\pi^2}(k - 2\mu)\right)(1 + \frac{2}{k_1})\delta}}, & \text{2D} \end{cases} . \tag{36}$$

Hence, with a given value of the horizon radius δ, the value of s_0 can be calculated from the macroscopic fracture energy G_c once the value of k_1 is known. The parameter k_1 mainly controls the mechanical response in the post-peak regime and can be fitted from experimental results. It is worth noticing that the value of s_0 is here determined by setting $k_2 = 0$. Starting from this primary value, an improved value of s_0 can be iteratively identified by putting another value of k_2.

4. Adaptive coupling method

The non-local numerical method based on the state-based PD theory is suitable to dealing with progressive damage and cracking process in solid materials. For large scale problems, the computer time can be considerably high. On the other hand, for many engineering problems, cracking generally occurs inside some small zones. For example, during excavation of an underground cavity, damage and cracking are generated only in the close zone to the excavated cavity wall. There is no need to use the damage model with the PD theory in far field. In this case, it is generally more efficient to use the classical finite element method for solving elastic (even plastic without softening and localization) problems in far field. Therefore, it is very convenient to combine the non-local PD theory for dealing with cracking process and the finite element method (FEM) for dealing with classical elastic and plastic problems. Further, it is also needed to consider that the size of cracking zone progresses during loading history. The boundary between the PD and the FEM zones is then not fixe but evolves. For this purpose, an adaptive coupling algorithm is here developed. In order to achieve such an adaptive coupling problem with moving PD-FEM boundary, two issues should be addressed: *when* the coupling is needed and *how* the coupling is realized.

In the present study, we shall develop an adaptive switching strategy. It is based on the relative elongation of the bond linking two adjacent FEM nodes (exactly the same as the stretch calculation defined in (17)). More precisely, the proposed coupling method is illustrated in Figure 5. One considers two initial FEM nodes (the gray square nodes) x_k and x_j. When the relative elongation between these nodes reaches a switching threshold value (Zaccariotto et al., 2018), they are converted to PD points together with all other points inside their horizon zones (the blue circle nodes). With the new bond damage model presented above, the switching threshold value is set as the bond stretch elastic limit s_0. In this way, the switching from FEM nodes to PD points is consistent with the crack propagation process. After the switching is turned on, the computational domain is divided into three regions (as shown in Figure 5b): the original FEM region, referring to the region composed of the quadrilateral elements with four gray square FEM nodes connected by the gray straight solid lines; the pure PD region, referring to the region including the blue circle PD points interacting with other PD points through the bonds indicated by the magenta curved solid lines; and the coupling region, referring to the region consisting of the nominal quadrilateral elements with FEM nodes and PD points connected by the gray straight dotted lines and solid lines, and the nominal bonds interacting PD points and FEM nodes indicated by the magenta curved dotted lines.

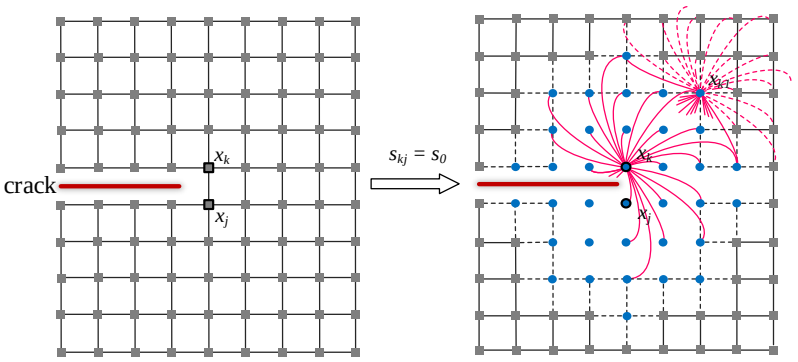

(a) Initial state (b) Coupling state

Figure 5: Diagram of adaptive coupling strategy: gray square nodes are FEM nodes and blue circle nodes are PD points; the gray straight solid lines represent the edges of the quadrilateral element in FEM, while the gray straight dotted lines represent the edges of the nominal elements in coupling region; the magenta curved solid lines indicate the PD bonds (the short magenta lines represent the bonds omitted for brevity), and the magenta curved dotted lines indicate the nominal bonds in coupling region.

For the effective realization of FEM-PD coupling, the static equilibrium equation of a PD point is first written as follows by substituting (22) for (5), it is:

$$\mathbf{0} = \sum_{j=1}^{N} \zeta_{kj} \left(4b\delta s_{kj} + \frac{2ad^2\delta^2}{|\boldsymbol{x_j} - \boldsymbol{x_k}|} \left(\sum_{m=1}^{N} \zeta_{km} s_{km} V_m + \sum_{n=1}^{N} \zeta_{jn} s_{jn} V_n \right) \right) V_j \frac{\boldsymbol{x_j} - \boldsymbol{x_k}}{|\boldsymbol{x_j} - \boldsymbol{x_k}|} + \boldsymbol{b}(\boldsymbol{x_k}) \tag{37}$$

Referring to the definition of stretch s of two pairwise points given in (17), and by means of the multiplier V_k representing the volume of material point $\boldsymbol{x_k}$, the equilibrium equation at $\boldsymbol{x_k}$ can be rewritten as:

$$\sum_{j=1}^{N} \zeta_{kj} \left(\frac{4b\delta V_j V_k}{|\boldsymbol{x_j} - \boldsymbol{x_k}|} (\boldsymbol{u_k} - \boldsymbol{u_j}) + \sum_{m=1}^{N} \zeta_{km} \frac{2ad^2\delta^2 V_m V_j V_k}{|\boldsymbol{x_j} - \boldsymbol{x_k}||\boldsymbol{x_m} - \boldsymbol{x_k}|} (\boldsymbol{u_k} - \boldsymbol{u_m}) + \sum_{n=1}^{N} \zeta_{jn} \frac{2ad^2\delta^2 V_n V_j V_k}{|\boldsymbol{x_j} - \boldsymbol{x_k}||\boldsymbol{x_n} - \boldsymbol{x_j}|} (\boldsymbol{u_j} - \boldsymbol{u_n}) \right) = \boldsymbol{b}(\boldsymbol{x_k}) V_k \tag{38}$$

Observing (38), it is seen that the equilibrium equation of a PD material point has a similar expression to that of FEM nodes:

$$\boldsymbol{K}_k^P \boldsymbol{U} = \boldsymbol{f}_k \tag{39}$$

in which $\boldsymbol{K}_k^P$ is treated as the stiffness components of the PD material point $\boldsymbol{x_k}$, it is defined as:

$$\boldsymbol{K}_k^P = \sum_{j=1}^{N} \begin{bmatrix} \cdots & \zeta_{kj} \left(p_1 + \sum_{m=1}^{N} \zeta_{km} p_2 \right) & \cdots & \zeta_{kj} (-\zeta_{km} p_2) & \cdots & \zeta_{kj} \left(-p_1 + \sum_{n=1}^{N} \zeta_{jn} p_3 \right) & \cdots & \zeta_{kj} (-\zeta_{jn} p_3) & \cdots \end{bmatrix} \tag{40}$$

where $p_1 = \frac{4b\delta V_j V_k}{|\boldsymbol{x_j} - \boldsymbol{x_k}|}$, $p_2 = \frac{2ad^2\delta^2 V_m V_j V_k}{|\boldsymbol{x_j} - \boldsymbol{x_k}||\boldsymbol{x_m} - \boldsymbol{x_k}|}$, $p_3 = \frac{2ad^2\delta^2 V_n V_j V_k}{|\boldsymbol{x_j} - \boldsymbol{x_k}||\boldsymbol{x_n} - \boldsymbol{x_j}|}$. Correspondingly, $\boldsymbol{U}$ represents the node displacement vector, which is given as:

$$\boldsymbol{U}^T = \begin{bmatrix} \cdots & \boldsymbol{u_k} & \cdots & \boldsymbol{u_m} & \cdots & \boldsymbol{u_j} & \cdots & \boldsymbol{u_n} & \cdots \end{bmatrix} \tag{41}$$

Finally $\boldsymbol{f}_k = \boldsymbol{b}(\boldsymbol{x_k})V_k$ denotes the external load acting on $\boldsymbol{x_k}$. Then owing to the expression in (39), the coupling can be realized by assembling the stiffness components respectively from FEM nodes and PD points into the global stiffness matrix (Galvanetto et al., 2016, Zaccariotto et al., 2018):

$$\boldsymbol{K} = \boldsymbol{K}^F + \boldsymbol{K}^P \tag{42}$$

where $\boldsymbol{K}$ denotes the global stiffness matrix. $\boldsymbol{K}^P$ denotes the stiffness matrix from the PD points as described in (40). $\boldsymbol{K}^F$ represents the stiffness matrix from FEM nodes, which is obtained by the classical assemblage of the elementary stiffness matrices $\boldsymbol{K}_e^F$ as follows (Zienkiewicz et al., 1977):

$$\boldsymbol{K}_e^F = \int \boldsymbol{B}^T \boldsymbol{D}\boldsymbol{B} dV \tag{43}$$

where $\boldsymbol{B}$ is the elementary displacement dradient matrix, and $\boldsymbol{D}$ denotes the elastic stiffness matrix for the FEM zones. It is worth noticing that the internal forces evaluated with the FEM only act on the FEM nodes, while the internal forces calculated using the PD theory are applied on the PD nodes. In other words, the internal force acting on a node is of the same nature as the node (Zaccariotto et al., 2018). Subsequently, the total system of equilibrium equations can be expressed as follows (Galvanetto et al., 2016, Zaccariotto et al., 2018):

$$\boldsymbol{K}\,\boldsymbol{U} = \boldsymbol{F} \tag{44}$$

$\boldsymbol{F}$ represents the total nodal force vector, which is assembled from the elementary nodal force vectors $\boldsymbol{F}_e$ given in the classical FEM framework (Zienkiewicz et al., 1977):

$$\boldsymbol{F}_e = \int \boldsymbol{N}^T \boldsymbol{p}_v dV + \int \boldsymbol{N}^T \boldsymbol{p}_s dS \tag{45}$$

where $\boldsymbol{N}$ is the matrix of shape functions, $\boldsymbol{p}_v$ denotes the body force vector, $\boldsymbol{p}_s$ the surface traction on the external boundary. With this system in hand, the nodal displacements can be determined by:

$$\boldsymbol{U} = \boldsymbol{K}^{-1}\,\boldsymbol{F} \tag{46}$$

Finally, the numerical method for modeling the progressive failure process in cohesive materials by using the new bond damage model and the adaptive FEM-PD coupling is established and illustrated in Algorithm 1.

Algorithm 1: Flowchart of the adaptive PD-FEM coupling algorithm

Input: E, ν, G_c , δ, $\Delta load$, k_1, k_2, s_0
Output: $\boldsymbol{U}_n$, $\boldsymbol{f}_n$, φ_n
Initialize $\boldsymbol{U}_n = \boldsymbol{U}_{n-1}$ ($\boldsymbol{U}_1 = \boldsymbol{0}$);
Calculate the relative elongation s of any two adjacent FEM nodes with (17);
if $s < s_0$ **then**
    Assemble the global stiffness matrix with (42) but $\boldsymbol{K}^P = \boldsymbol{0}$;
else
    Update the PD nodes set based on the adaptive switching strategy;
    Calculate the bond stretch value s_{kj} with (17);
    Calculate the bond status value ζ_{kj} with (27);
    Assemble the global stiffness matrix with (40), (42) and (43);
end
Solve the system of equilibrium equations and obtain the node displacements $\boldsymbol{U}_n$ with (46);
Update the PD bond stretch value s_{kj} with (17);
Update the PD bond status value ζ_{kj} with (27);
Calculate the global damage value φ_n of PD points with (25).

5. Numerical assessment and experimental validation

The proposed numerical method is implemented with the MATLAB software. In this section, a few linear elastic examples with a fixed PD region are first considered to assess the accuracy of the proposed coupling method. Then several typical experimental tests on concrete structures are investigated to verify the efficiency of the new bond damage model implemented with the adaptive PD-FEM coupling method for modeling the progressive failure process in cohesive materials. In those cases, the PD region is no more fixed a priori but depends on the evolution of cracking process. All the numerical calculations are performed in 2D plane stress conditions using uniform meshes composed of quadrilateral elements. The unit of all length variables is millimeter (mm).

5.1. Elastic response verification

We consider first two linear elastic examples to verify the accuracy of the proposed FEM-PD coupling method. The first example is a uni-dimensional bar subjected to tensile force. As shown in Figure 6, the bar with a length of $50mm$ is constrained at the left end (which is set to the origin of the coordinates frame), and is stretched by a unit force $F(F = 1N)$ at the right end. The cross section area is $A = 1mm^2$. For the mesh, the bar is divided by a uniform grid space Δ. The selected value of Young's nodulus is $E = 1GPa$. For the FEM-PD coupling, the region of $20 \leq x \leq 30$ (the area filled with pink color) is chosen for the PD modeling. And the horizon radius δ is specified as $\delta = 3\Delta$, as widely used in previous studies (Zaccariotto et al., 2017, Madenci and Oterkus, 2017, Gao and Oterkus, 2019). In order to explore the robustness sensitivity of the adopted coupling method with respect to the grid size, three cases respectively with $\Delta = 2mm$, $\Delta = 1mm$ and $\Delta = 0.5mm$ are considered. For each case, the solutions obtained by the coupled FEM-PD method and from the pure FEM modeling are compared with the analytical ones. From Figure 7, it can be observed that

the displacements obtained by the FEM calculation and by the coupled method perfectly coincide with the analytical solutions. It seems to confirm the effectiveness of the developed state-based PD method as well as the FEM-PD coupling strategy. Moreover, the numerical results are not dependent on the grid size.

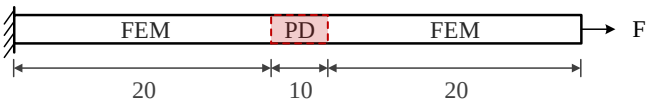

Figure 6: Geometry and boundary conditions of the 1D bar problem

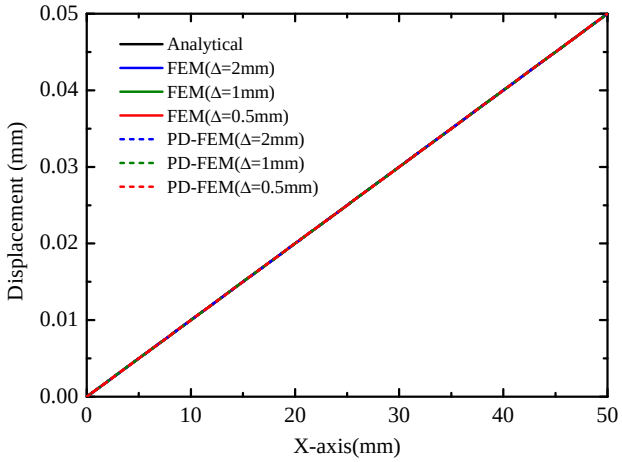

Figure 7: Comparisons of node displacements for the 1D bar problem

In the second example, two rectangular plates are studied. Their geometry and boundary conditions are depicted in Figure 8. In the second plate, a notch with a size of $5mm \times 1mm$ is pre-set on the upper edge and at a distance of $2mm$ from the horizontal symmetry axis *line 1′*. Both of the plates are fixed at the left edge, and are subjected to a uniformly distributed shear force ($P = -1N/mm$) at the right edge. The plate thickness is $h = 1mm$. The selected values of elastic parameters are: Young's nodulus $E = 1GPa$ and Poisson's ratio $\nu = 0.2$. The two plates are uniformly meshed by the quadrilateral elements with a size of $\Delta x = \Delta y = \Delta$. For the plate without notch, the filled region with a range of $20 \leq x \leq 30, 0 \leq y \leq 20$ is set as the PD region. And for the notched plate, the PD nodes are in the region of $20 \leq x \leq 30, 0 \leq y \leq 15$. The horizon radius δ is also taken as three times of the grid length Δ. Again, the different grid size are chosen as $\Delta = 1mm$, $\Delta = 0.5mm$ and $\Delta = 0.25mm$. The displacement solutions given by pure FEM calculation and the coupling FEM-PD method are compared along the geometric centerlines (*line 1* and *line 2* for the plate without notch, and along the lines *line 1′* and *line 2′* for the notched plate). The obtained results are present in Figure 9 and Figure 10 respectively. It can be seen that the results based on the coupling method are well consistent with those by the FEM calculation for all the cases. However, it is undeniable that the grid size does have a certain impact on the results. In general, the relative error between the coupling method and the FEM calculation decreases with the decrease of the grid size. For the two cases studied here, the relative

error between the two calculations is less than 2%. On the other hand, the maximum relative error between three grid sizes for the results obtained by the FEM-PD coupling method is about 3%.

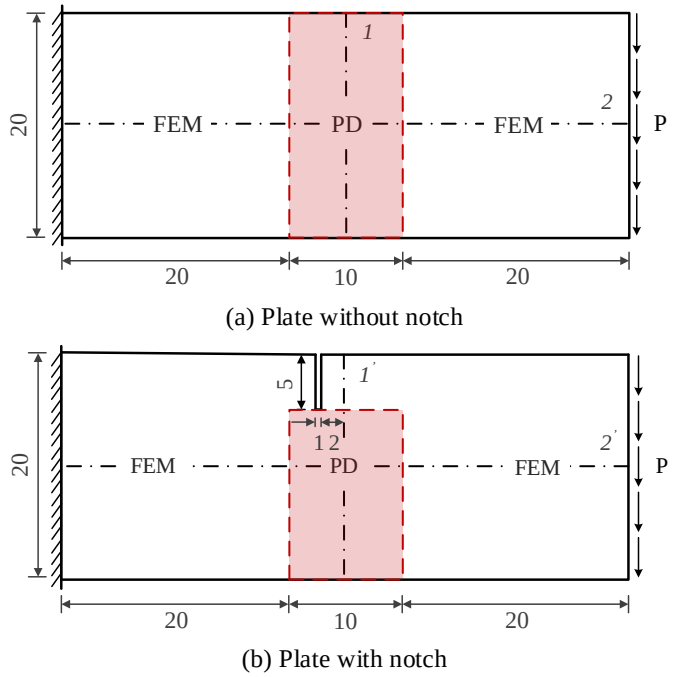

(a) Plate without notch

(b) Plate with notch

Figure 8: Geometry and boundary conditions of the 2D plate problems

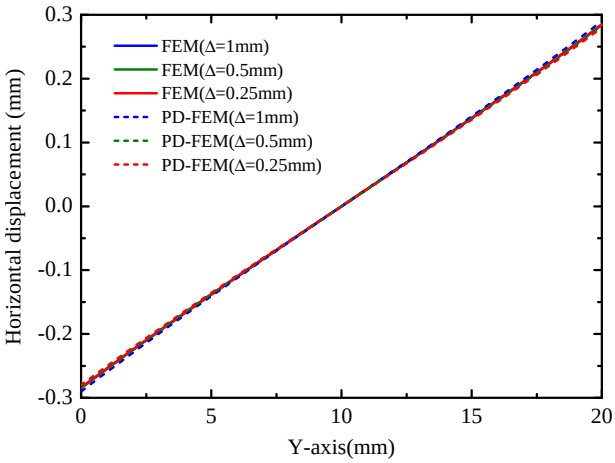

(a) Horizontal displacements along *line 1*

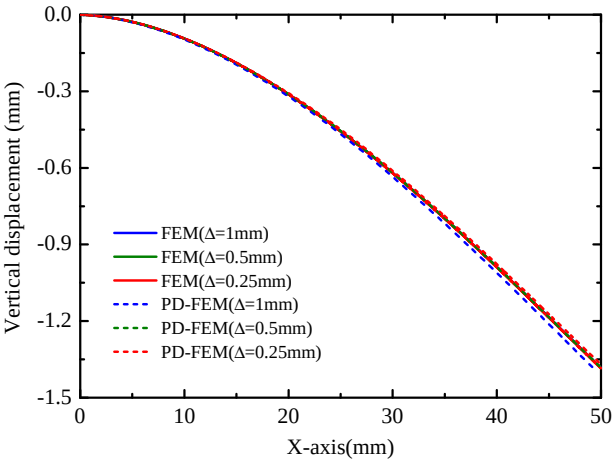

(b) Vertical displacements along *line 2*

Figure 9: Nodal displacements of the plate without notch

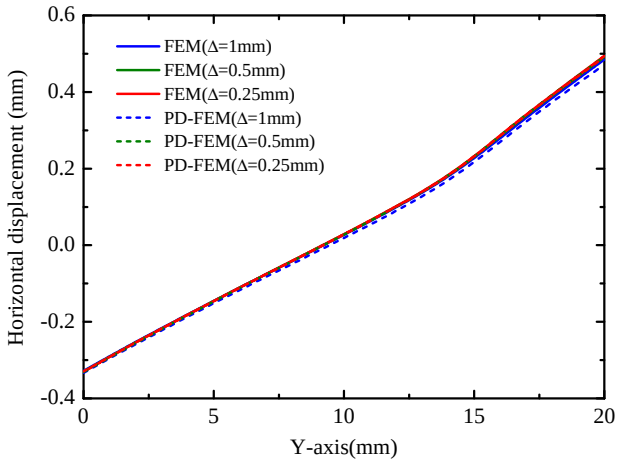

(a) Horizontal displacements along *line 1′*

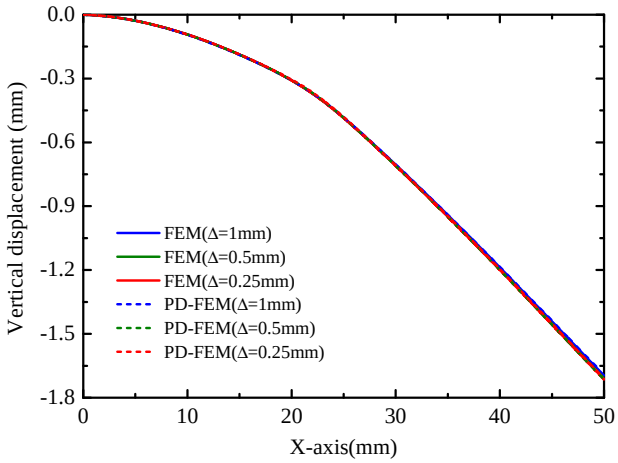

(b) Vertical displacements along *line 2′*

Figure 10: Nodal displacements of the notched plate

5.2. *Wedge splitting test*

We shall now assess the ability of the proposed FEM-PD coupling method for modeling the progressive failure process.

The first example considered is the wedge splitting test of a concrete specimen CP250 reported in (Trunk, 1999), and widely used to investigate mode-I fracture process. The geometric and boundary conditions of the test are presented in Figure 11. The notched specimen is subjected to the symmetrically prescribed displacement (u) at the middle point of the upper notch. The material properties are taken from the previous study (Trunk, 1999): Young's modulus $E = 28.3GPa$, Poisson's ratio $\nu = 0.18$ and fracture energy $G_c = 0.3N/mm$. The grid size of the adopted mesh is $\Delta = 5mm$. And the horizon radius δ is equal to 3Δ.

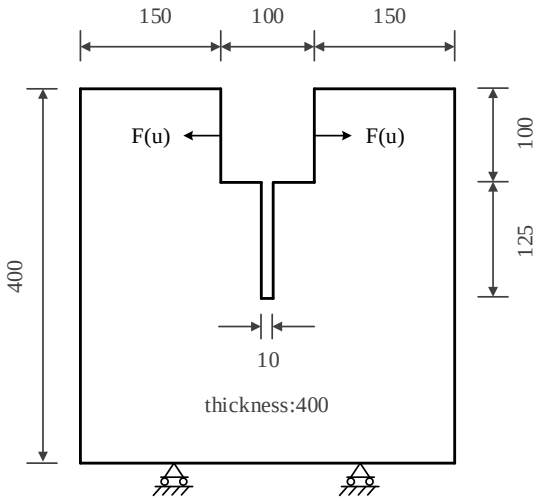

Figure 11: Geometrical and boundary conditions of the wedge splitting test

5.2.1. Sensitivity analysis of bond damage parameters

The sensitivity of numerical results to the key parameters involved in the new bond damage model is first evaluated. As described in Section 3, there are three key parameters introduced in the proposed bond damage model, which are k_1, k_2 and s_0. s_0 can be determined from k_1 and k_2 according to (30) and (31). In consequence, the parameters that play the major role are k_1 and k_2. Numerical calculations are then performed with different values of those parameters in order to verify their impacts on the obtained numerical solutions.

The influence of k_1 is first studied by taking $k_1 = 0.02$, $k_1 = 0.01$ and $k_1 = 0.005$, while keeping k_2 to 0. From Figure 12, one can see that k_1 not only affects the peak value of structure strength but also controls the reduction rate of force after the peak value. The peak strength decreases when the value of k_1 is smaller. This is due to the fact that the bond stretch elastic limit s_0 decreases when k_1 is smaller as predicted by (36). As a consequence, the cracking process starts earlier. On the other, the parameter k_1 does not affect the residual strength. Accordingly, when its value is higher, as the peak strength is higher, one gets a more rapid drops of force after the peak strength.

Three different values of k_2 (k_2=0, $k_2 = 0.02$, $k_2 = 0.05$) are also considered by taking $k_1 = 0.005$. The obtained force-displacement curves are depicted in Figure 13. One observes a quasi uniform increase of both the peak and residual strengths when the value of k_2 increases. It does not affect the reduction rate of force in the post-peak regime. According to (26) and (27), the bond damage rate is lowered by a higher value of k_2. This leads to the increase of the peak and residual strengths.

As mentioned above, the value of s_0 is theoretically calculated by suing (36). However, several assumptions are used to reach the simplified form of (36). Therefore, it appears interesting to evaluate the sensitivity of numerical results to any perturbation of s_0. For this purpose, the reference value of s_0 is first calculated by (36). Then, two other disturbed values are selected as $s_{01} = 1.10s_0$ and $s_{02} = 1.05s_0$. The values of k_1 and k_2 are hold constant in three cases ($k_1 = 0.005$, k_2=0). The obtained results are shown in

Figure 14. One can see that the influence of s_0 is a kind of mixture of those of k_1 and k_2. The values of s_0 affects significantly the peak strength and slightly the residual strength.

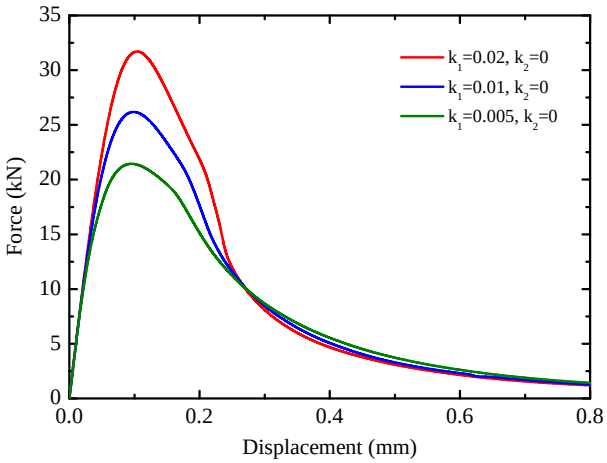

Figure 12: Sensitivity analysis of k_1 with $k_2 = 0$

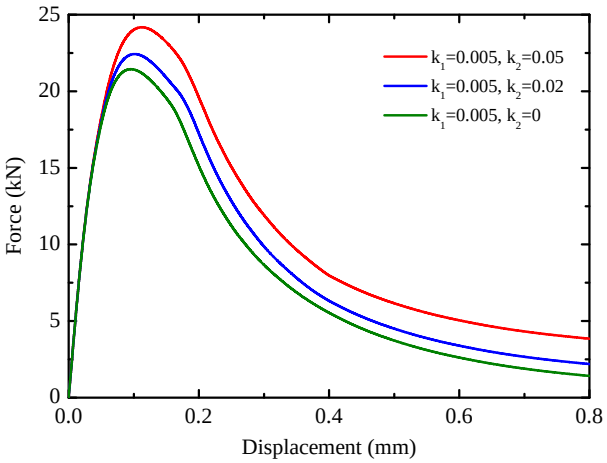

Figure 13: Sensitivity analysis of k_2 with $k_1 = 0.005$

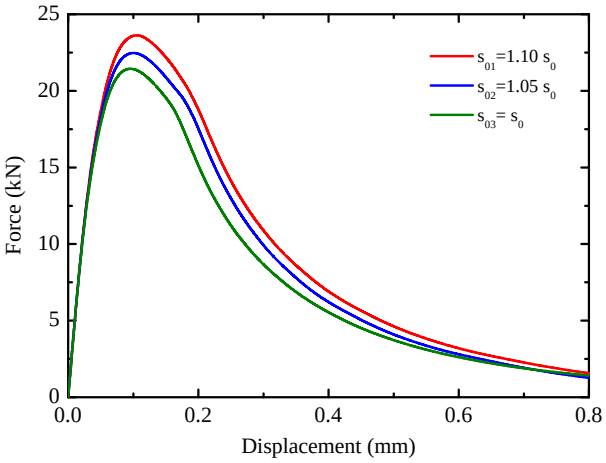

Figure 14: Sensitivity analysis of s_0 with $k_1 = 0.005$,$k_2 = 0$

5.2.2. *Sensitivity analysis of loading increment size*

Crack propagation is a strongly nonlinear problem. The whole loading history is divided into a number of loading steps. Increments of forces and displacements are prescribed at each loading step. Due to the strong nonlinearity, numerical solutions can be significantly influenced by the size of load increment. For this purpose, the influence of the prescribed displacement increment size (Δu) is here evaluated by taking four different values. As presented in Figure 15, the size of (Δu) has a significant impact on the overall force-displacement responses. Large sizes of Δu, such as $\Delta u = 5 \cdot 10^{-3} mm$, may delay and under-estimate cracking process and generates numerical oscillations. However, the numerical results are convergent when the size of Δu is small enough. For instance, the numerical results seem to become stable when the size of Δu is about $5 \cdot 10^{-4} mm$ or less.

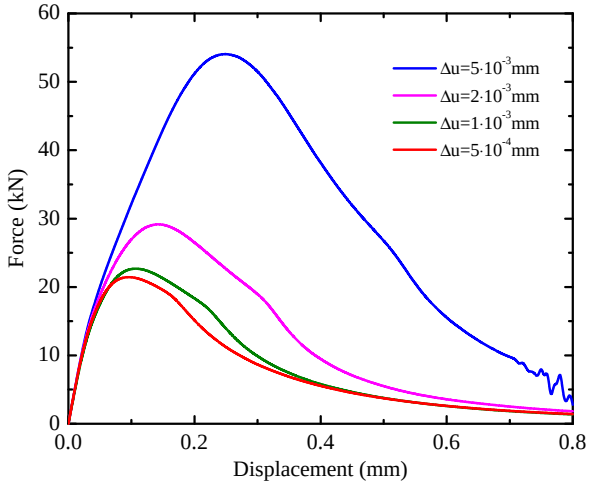

Figure 15: Convergence study of overall response for wedge splitting test with respect to displacement increment size Δu ($k_1 = 0.005$, $k_2 = 0$)

5.2.3. *Experimental verification*

The numerical results are now compared with the experimental data reported in (Trunk, 1999) in terms of overall force-displacement curves. For the parameters involved in the bond damage model, the value of k_1 is adjusted to 0.005. Two values of k_2 are chosen as 0, 0.02. The adopted value of s_0 is 10% higher than the calculated one by (36). This is consistent with the fact that the value of s_0 is slightly under-estimated by (36) due to the simplifications made. The size of the prescribed displacement increment us $\Delta u = 5 \cdot 10^{-4} mm$ based on the sensitivity study presented above.

As shown in Figure 16a, the numerical results obtained by using the new bond damage model associated with the coupled FEM-PD method are in good agreement with the experimental data. Particularly, the progressive reduction of force in the post-peak regime is well described. The use of k_2 in the new bond damage model improves the numerical results and enlarges the model's ability, for both the peak and residual strengths. For further outlining the advantage of the new bond damage model, the numerical results based on the classical PMB model are presented in Figure 16b. It is clear that there are large scatters with the experimental results. The classical PMB model overestimates the peak strength and the reduction rate of force in the post-peak regime while the residual strength is underestimated. Furthermore, some numerical oscillations are also observed in the results given by the PMB model.

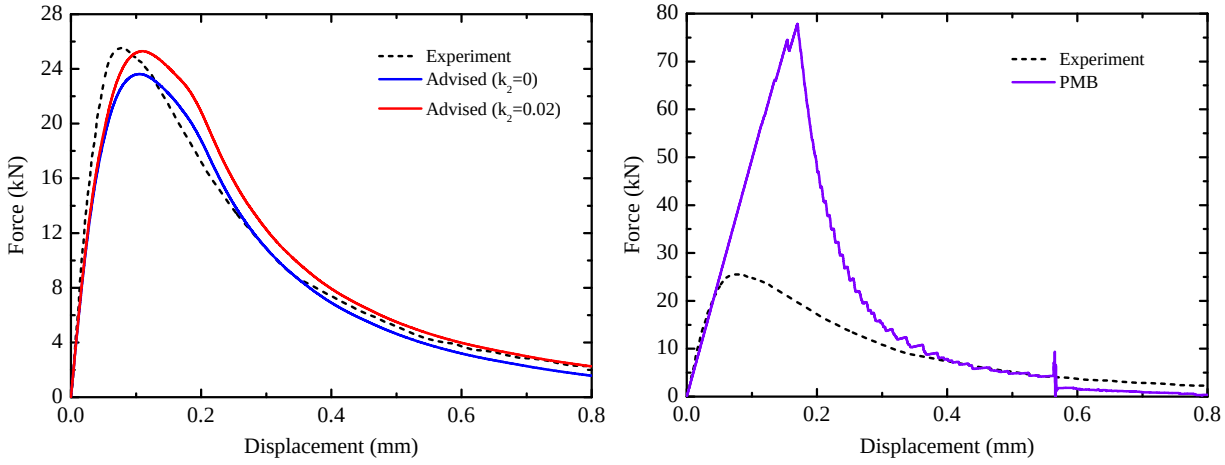

(a) Advised damage model

(b) PMB damage model

Figure 16: Comparisons of force-displacement curves of wedge splitting test between different bond damage models and experimental data ((Trunk, 1999))

The crack propagation process in the wedge splitting test is also investigated. The overall damage distributions are calculated and presented in Figures 17 and 18 at four subsequent loading steps ($u = 0.1mm$, $u = 0.2mm$, $u = 0.4mm$, $u = 0.8mm$), and respectively for two values of k_2 ($k_2 = 0$, $k_2 = 0.02$). One can see that in both cases the cracking emerges and propagates vertically along the symmetric line during the loading history. This is consistent with the experimental observations reported in (Trunk, 1999). Comparing the two cases, it is concluded that the residual strength parameter k_2 hardly affects the crack propagation pattern,

but slightly reduces the maximum damage value.

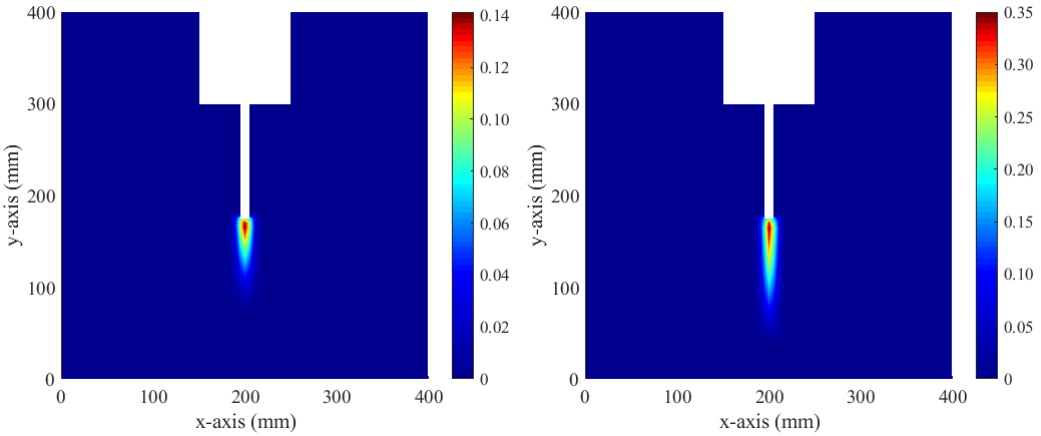

(a) u=0.1mm (b) u=0.2mm

(c) u=0.4mm (d) u=0.8mm

Figure 17: Global damage value contours in wedge splitting test ($k_2 = 0$)

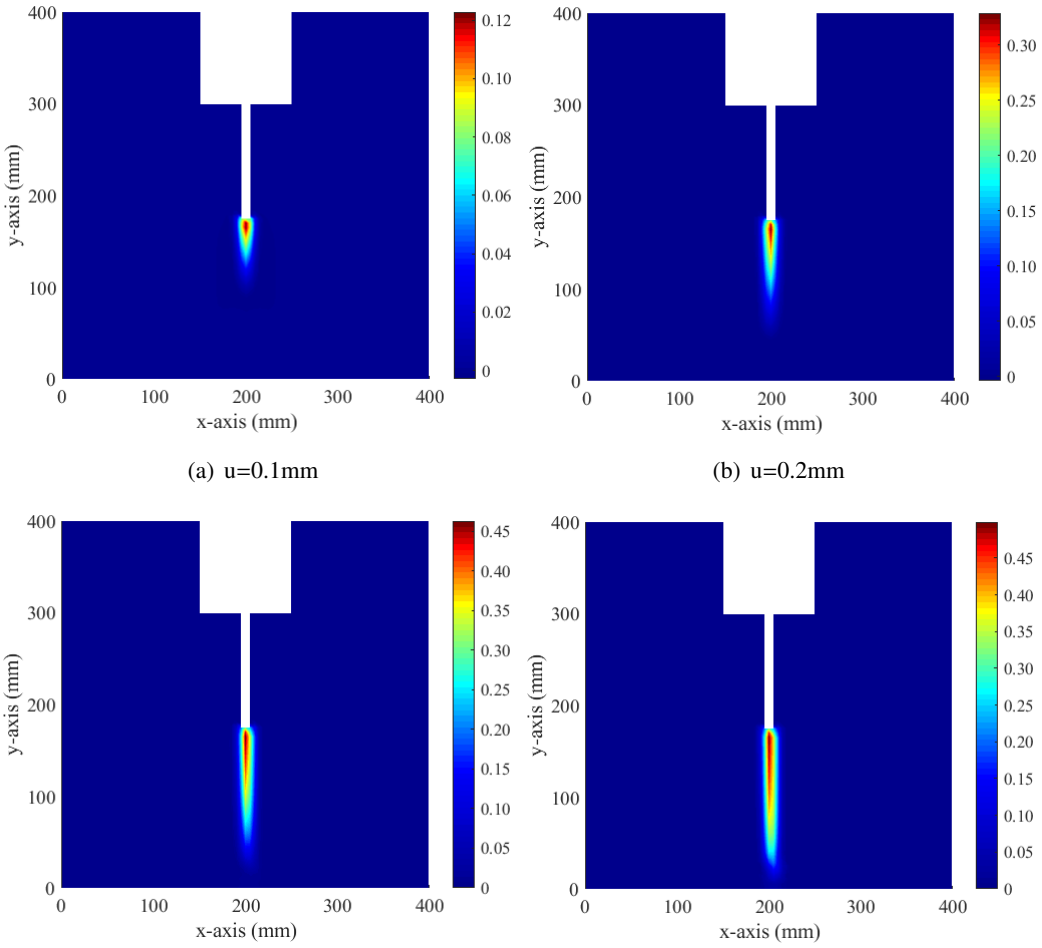

(a) u=0.1mm (b) u=0.2mm

(c) u=0.4mm (d) u=0.8mm

Figure 18: Global damage value contours in wedge splitting test ($k_2 = 0.02$)

5.3. L-shape test

The second case is a mixed-mode test of an L-shaped concrete structure illustrated in Figure 19. This test was carried out in (Winkler et al., 2001). As set in the experiment, a vertical displacement is applied to the point at a distance of $30mm$ from the right edge while the fixed constraints are prescribed on the bottom edge. Based on previous studies (Winkler et al., 2001, Le et al., 2018), the mechanical parameters chosen are Young's modulus $E = 25.85GPa$, Poisson's ratio $\nu = 0.18$ and critical fracture energy $G_c = 0.065N/mm$. For the mesh, the grid size is set as $\Delta = 5mm$. The horizon radius δ is again equal to 3Δ.

In the numerical calculation, the size of applied displacement increment is chosen as $10^{-3}mm$. The damage parameter k_1 is taken as 0.01. The value of s_0 is adjusted to 1.5 times the value given by (36). The obtained force-displacement curves for $k_2 = 0$ and $k_2 = 0.02$ are shown in Figure 20a. In an overall manner, the numerical results agree well with the experimental data, especially for the response in the post-peak region. Again, the results based on the PMB model are presented in Figure 20b. Once more, large scatters

with experimental data are observed. The PMB model predicts a too high peak strength and a too stiff (or brittle) behavior in the post-peak region. The advantage of the new bond damage model in modelling the progressive failure of cohesive materials is again clearly demonstrated.

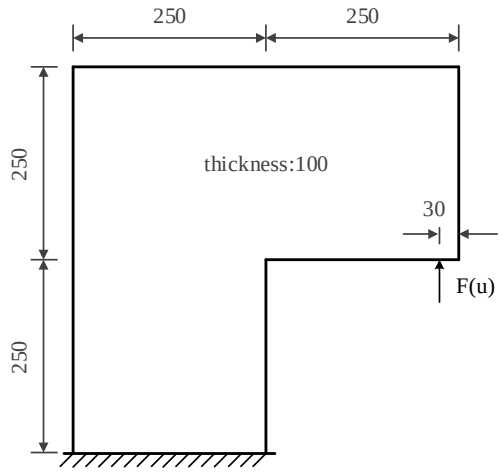

Figure 19: Sketch map of the L-shape test

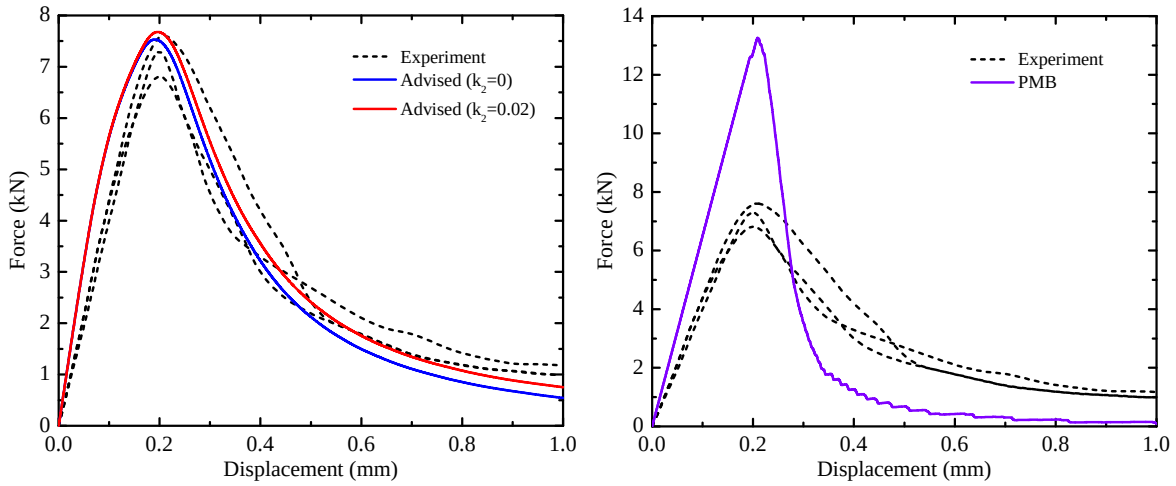

(a) Advised damage model

(b) PMB damage model

Figure 20: Comparisons of force-displacement curves of L-shape test between different damage models and experimental data ((Winkler et al., 2001))

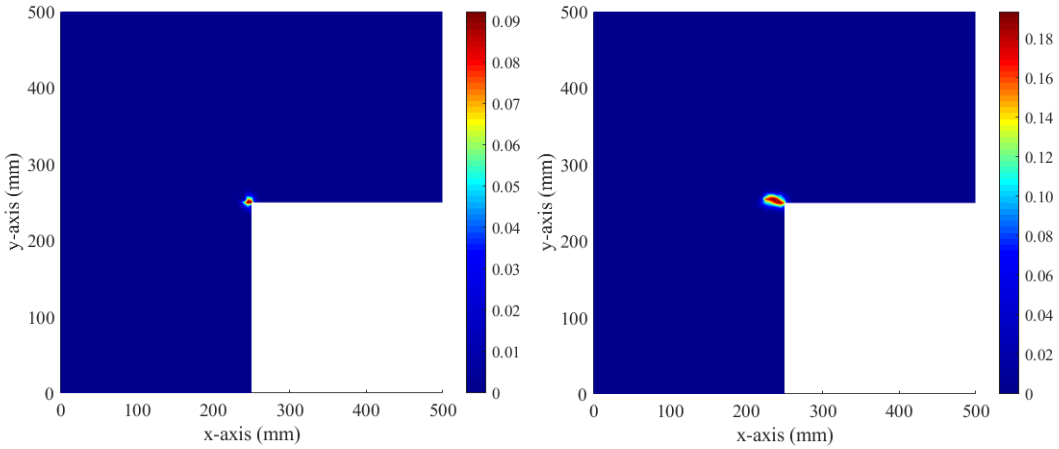

(a) u=0.1mm

(b) u=0.2mm

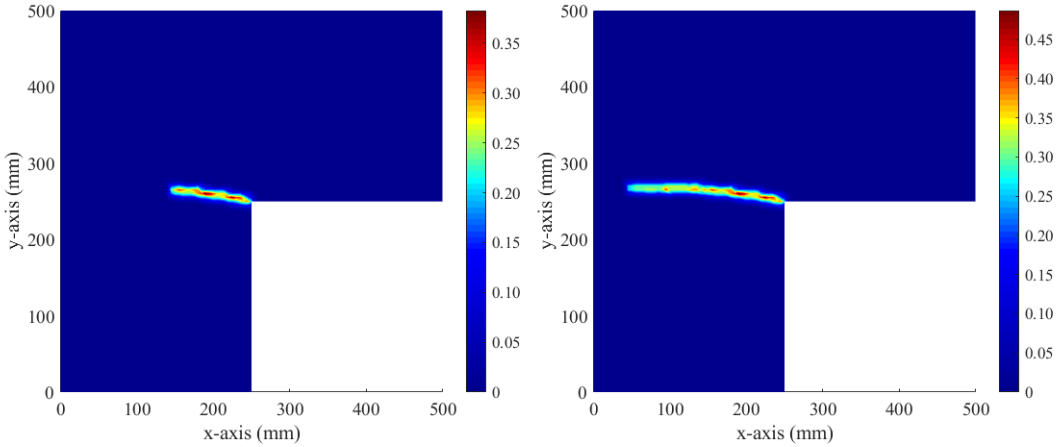

(c) u=0.3mm

(d) u=0.5mm

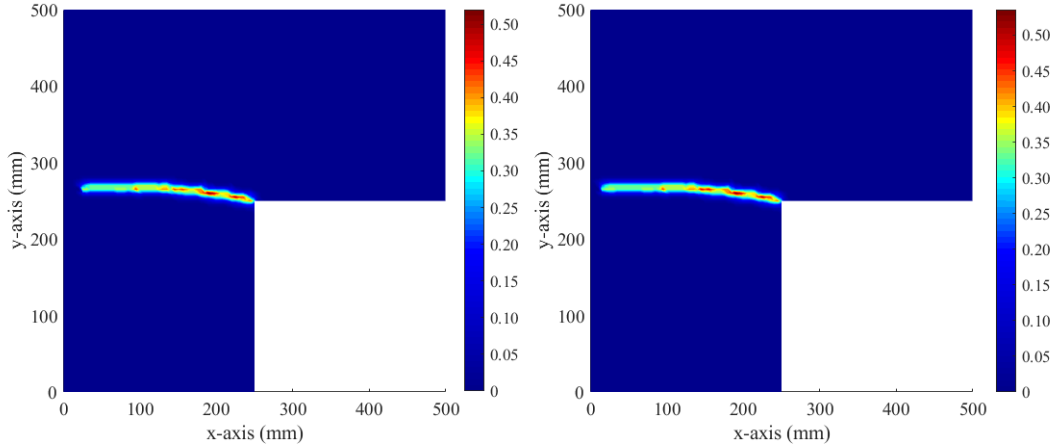

(e) u=0.8mm

(f) u=1mm

Figure 21: Global damage value contour in L-shape test (k_2 = 0.02)

The crack propagation patterns are illustrated in Figure 21 in terms of the overall damage contour at different loading steps for the case $k_2 = 0.02$. As it can be found, the crack initiates from the corner and then curvedly propagates toward the left side. This coincides well with the experimentally observed results in (Winkler et al., 2001), particularly the curved cracking path. Moreover, in Figure 22, one presents the cracking paths predicted by the bond and state based peridynamics theories and that observed in the experiment. On the whole, both numerical predictions are consistent with the experimental observation. But the smoothly curvilinear cracking path is better captured by the state-based peridynamics theory. It is noticed that by using the adaptive coupling method proposed here, the boundary between the PD and FEM zones is not fixed and evolves during the cracking process. For instance, for this example, at the initial state, all the domain belongs to the FEM nodes. With the nucleation and propagation of induced cracks, the PD zone is introduced. In Figure 23, one can see the current PD points distributions at u=1mm, which are surrounded by the FEM nodes.

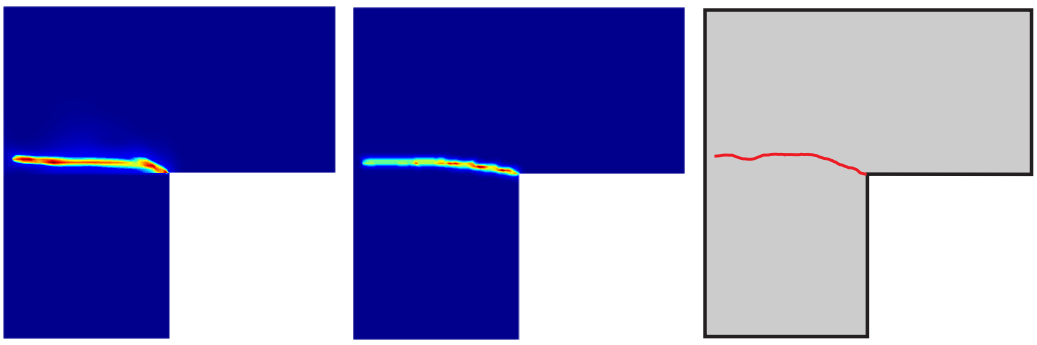

(a) bond-based PD (b) state-based PD (c) experiment

Figure 22: Comparisons of cracking path between bond-based PD, state-based PD and experiment observation ((Winkler et al., 2001))

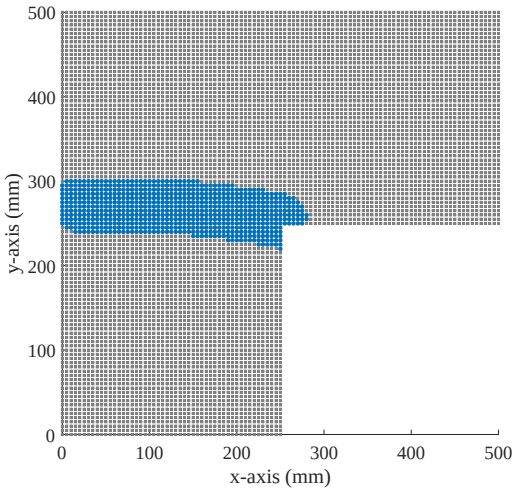

Figure 23: Illustration of PD and FEm zones at u=1mm: gray square for FEM nodes and blue circle for PD points

5.4. Tension-shear test

Finally, the combined tension-shear test performed in (Nooru-Mohamed et al., 1993) is investigated. The geometric parameters and boundary conditions of this test are shown in Figure 24. The double-edge notched specimen is under combined tension and shear. The specimen is firstly subjected to the lateral force $P_s = 5kN$ along the left edge above the notch, and then subjected to the axial tensile force at the top edge while P_s is maintained unchanged. The tensile force is applied in the form of displacement in order to capture the post-peak response. Based on previous studies (Wu et al., 2015, Zhang et al., 2015), the mechanical parameters are taken as: Young's modulus $E = 32GPa$, Poisson's ratio $\nu = 0.2$ and critical fracture energy $G_c = 0.11N/mm$. The grid size of adopted mesh is $\Delta = 1.25mm$ and the value of PD horizon radius δ is again chosen as 3Δ.

After preliminary calculations, the prescribed displacement increment is determined as $2 \cdot 10^{-4}mm$. Regarding the parameters in the new bond damage model, k_1 has a value of 0.002, two values (0 and 0.01) are assigned to k_2, and s_0 is 20% higher than the value calculated with (36).

The predicted force-displacement curves are presented in Figure 25. Both the peak strength value and the post-peak response are in good concordance with the experimental data. The use of the residual force parameter ($k_2 = 0.01$) improves the numerical prediction. The results obtained by the classical PMB model are once more significantly in disagreement with the experimental data.

In Figure 26, one illustrates the crack propagation modes by the overall damage contour at different loading steps for the case $k_2 = 0.01$. The experimental observations reported in (Nooru-Mohamed et al., 1993) are well reproduced. The crack initiates at the corner of the notch and propagates along a curvilinear path owing to the combined effect of lateral compression induced shear and axial tension.

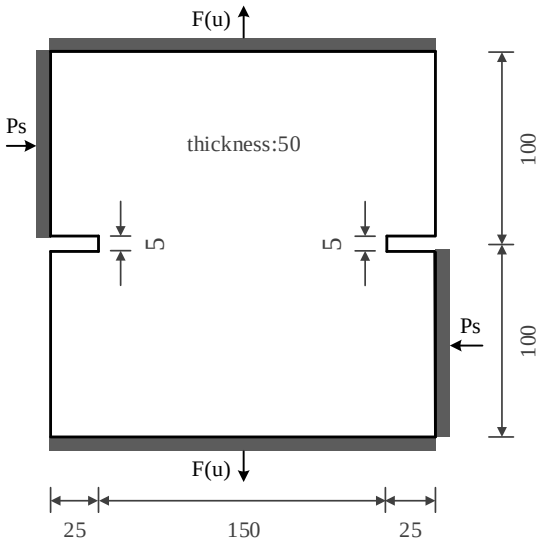

Figure 24: Geometrical parameters and boundary conditions of the tension-shear test

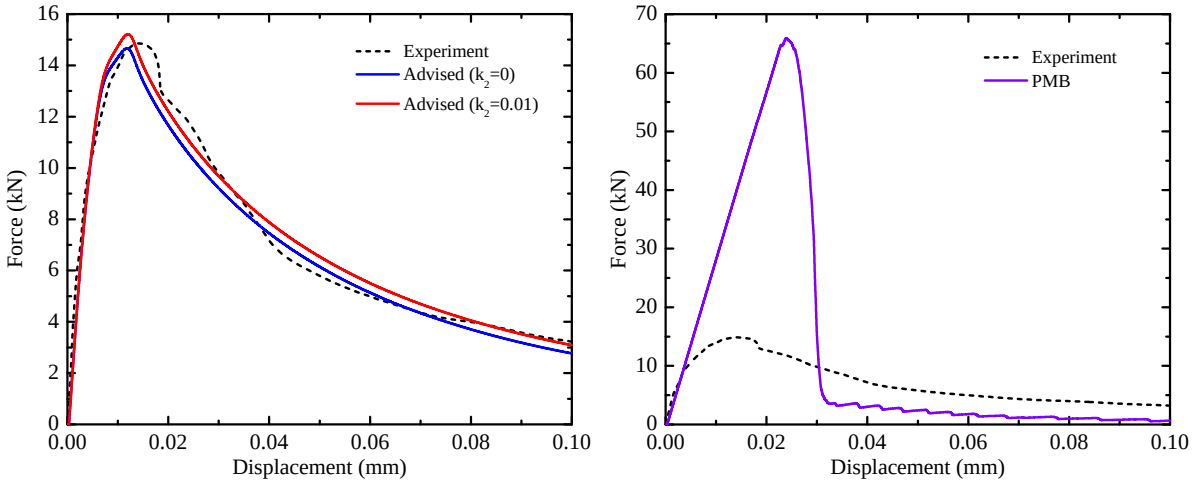

(a) Advised damage model (b) PMB damage model

Figure 25: Comparisons of force-displacement curves of tension-shear test between different bond damage models and experimental data (Nooru-Mohamed et al., 1993)

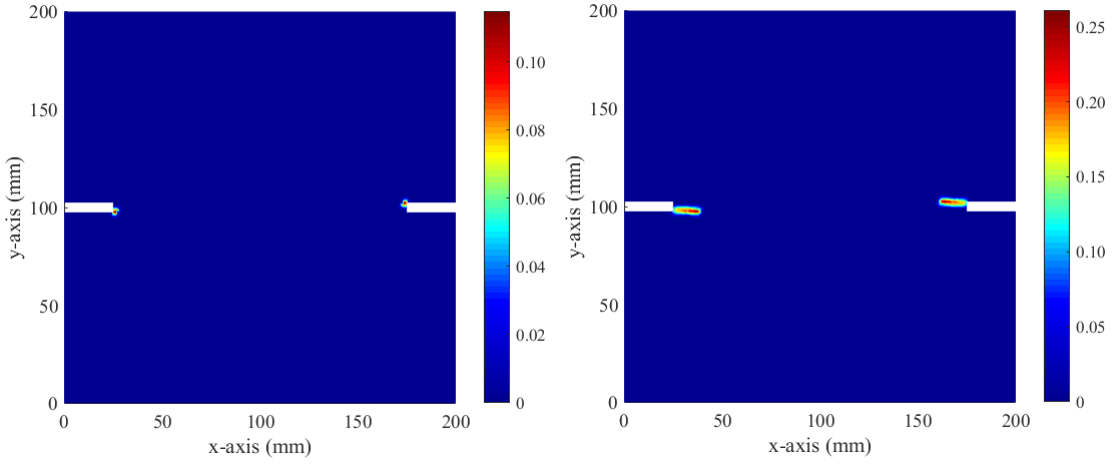

(a) u=0.01mm (b) u=0.02mm

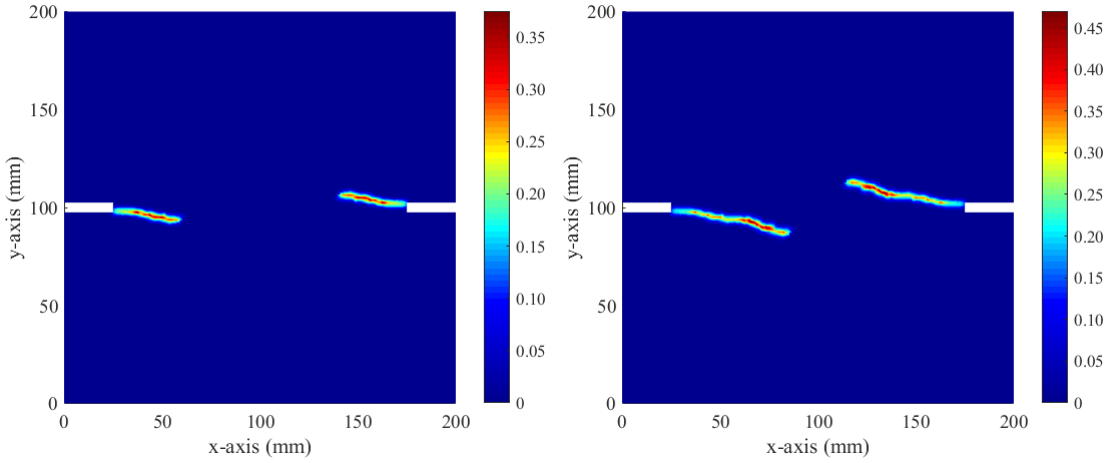

(c) u=0.03mm (d) u=0.05mm

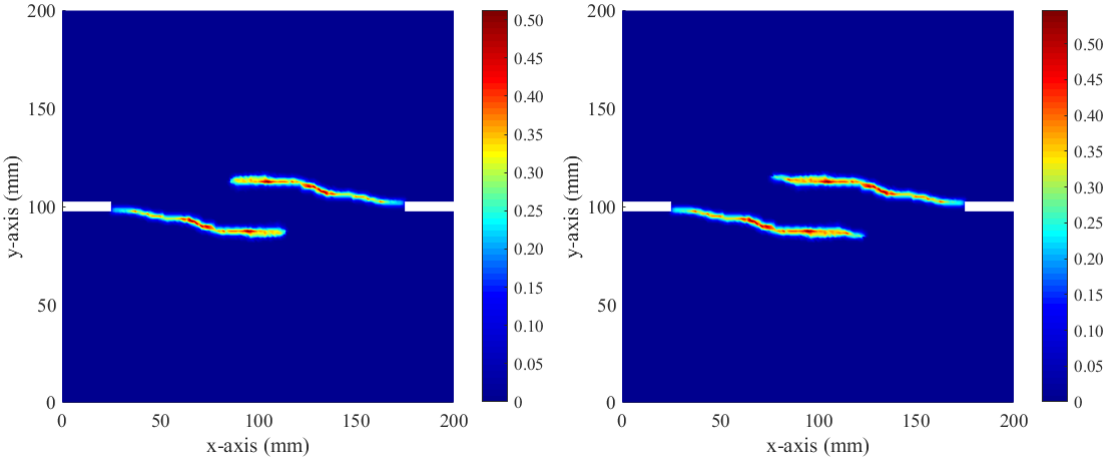

(e) u=0.08mm (f) u=0.1mm

Figure 26: Global damage value contour in tension-shear test (k_2 = 0.01)

6. Conclusions

In this paper, a new bond damage model has been proposed and implemented in the state-based peridynamics theory. This model describes the continuous degradation of bond strength and is able to take into account the bond residual strength. At the macroscopic scale, the new model is especially suitable for modeling the progressive failure process in cohesive materials and related structures. The local parameters introduced in the bond damage model can be directly related to the macroscopic elastic properties and critical fracture energy of materials. With these parameters, the proposed model provides a large ability in predicting the macroscopic peak strength, the post-peak response as well as the residual strength of structures.

An adaptive coupling strategy has also been developed for the combination of the state-based peridynamics theory and classical finite element method. The advantages of each method are conjugated for dealing with the progressive failure process in large scale structures. The PB theory based method is used for modeling localized cracking process while the FEM is particularly efficient for modeling elastic and plastic problems withour localization. Further, the adaptive switching method significantly increases the numerical efficiency for dealing with evolutive cracking domains. The accuracy of the proposed coupling method has been verified by the analytical solutions for some selected elastic examples.

The efficiency of the proposed bond damage model implemented in the adaptive coupling method has been validated through several representative tests on concrete structures, including the wedge splitting test, L-shape test and tension-shear test. Both tensile and mixed-mode cracking patterns have been observed in those tests. Both the force-displacement curves and the cracking trajectories have been correctly reproduced by the proposed method. Compared to the classical bond model, the advantages of the proposed method in predicting the peak strength and the progressive post-peak softening behavior have been clearly highlighted. In addition, it seems that the state-based PD theory is more suitable to described the curvilinear cracking path than the bond-based PD theory due to the simultaneous consideration of shear and volumetric strains. As future prospectives, the proposed method will be applied to numerical analysis of cracking process in large scale structures in order to highlight the efficiency of adaptive FEM-PD coupling strategy.

Acknowledgments

This work has been partially supported by the I-site program of University of Lille through the project Multifrac.

References

Bažant, Z. P., 1976. Instability, ductility, and size effect in strain-softening concrete. ASCE J Eng Mech Div 102 (2), 331–344.

Bažant, Z. P., 2002. Concrete fracture models: testing and practice. Engineering fracture mechanics 69 (2), 165–205.

Bazant, Z. P., Li, Y. N., 1997. Cohesive crack with rate-dependent opening and viscoelasticity: I. mathematical model and scaling. International Journal of Fracture 86 (3), 247–265.

Bie, Y. H., Cui, X. Y., Li, Z. C., 2018. A coupling approach of state-based peridynamics with node-based smoothed finite element method. Computer Methods in Applied Mechanics and Engineering 331, 675–700.

Dias-da Costa, D., Alfaiate, J., Sluys, L., Júlio, E., 2010. A comparative study on the modelling of discontinuous fracture by means of enriched nodal and element techniques and interface elements. International Journal of Fracture 161 (1), 97.

Diehl, P., Prudhomme, S., Lévesque, M., 2019. A review of benchmark experiments for the validation of peridynamics models. Journal of Peridynamics and Nonlocal Modeling, 1–22.

Foster, J. T., Silling, S. A., Chen, W., 2011. An energy based failure criterion for use with peridynamic states. International Journal for Multiscale Computational Engineering 9 (6).

Galvanetto, U., Mudric, T., Shojaei, A., Zaccariotto, M., 2016. An effective way to couple fem meshes and peridynamics grids for the solution of static equilibrium problems. Mechanics Research Communications 76, 41–47.

Gao, Y., Oterkus, S., 2019. Ordinary state-based peridynamic modelling for fully coupled thermoelastic problems. Continuum Mechanics and Thermodynamics 31 (4), 907–937.

Grassl, P., Jirásek, M., 2006. Damage-plastic model for concrete failure. International journal of solids and structures 43 (22-23), 7166–7196.

Hillerborg, A., Modéer, M., Petersson, P.-E., 1976. Analysis of crack formation and crack growth in concrete by means of fracture mechanics and finite elements. Cement and concrete research 6 (6), 773–781.

Hoover, C. G., Bažant, Z. P., 2014. Cohesive crack, size effect, crack band and work-of-fracture models compared to comprehensive concrete fracture tests. International Journal of Fracture 187 (1), 133–143.

Javili, A., Morasata, R., Oterkus, E., Oterkus, S., 2018. Peridynamics review. Mathematics and Mechanics of Solids, 1081286518803411.

Jirásek, M., 2000. Comparative study on finite elements with embedded discontinuities. Computer methods in applied mechanics and engineering 188 (1-3), 307–330.

Le, L. A., Nguyen, G. D., Bui, H. H., Sheikh, A. H., Kotousov, A., 2018. Localised failure mechanism as the basis for constitutive modelling of geomaterials. International Journal of Engineering Science 133, 284–310.

Li, Y.-N., Bažant, Z. P., 1994. Eigenvalue analysis of size effect for cohesive crack model. International Journal of fracture 66 (3), 213–226.

Macek, R. W., Silling, S. A., 2007. Peridynamics via finite element analysis. Finite Elements in Analysis and Design 43 (15), 1169–1178.

Madenci, E., Barut, A., Futch, M., 2016. Peridynamic differential operator and its applications. Computer Methods in Applied Mechanics and Engineering 304, 408–451.

Madenci, E., Dorduncu, M., Barut, A., Phan, N., 2018. A state-based peridynamic analysis in a finite element framework. Engineering Fracture Mechanics 195, 104–128.

Madenci, E., Oterkus, E., 2014. Peridynamic theory and its applications. Springer.

Madenci, E., Oterkus, S., 2017. Ordinary state-based peridynamics for thermoviscoelastic deformation. Engineering Fracture Mechanics 175, 31–45.

Miehe, C., Hofacker, M., Welschinger, F., 2010. A phase field model for rate-independent crack propagation: Robust algorithmic implementation based on operator splits. Computer Methods in Applied Mechanics and Engineering 199 (45-48), 2765–2778.

Moës, N., Belytschko, T., 2002. Extended finite element method for cohesive crack growth. Engineering fracture mechanics 69 (7), 813–833.

Moës, N., Dolbow, J., Belytschko, T., 1999. A finite element method for crack growth without remeshing. International journal for numerical methods in engineering 46 (1), 131–150.

Molnár, G., Gravouil, A., 2017. 2d and 3d abaqus implementation of a robust staggered phase-field solution for modeling brittle fracture. Finite Elements in Analysis and Design 130, 27–38.

Ni, T., Zaccariotto, M., Zhu, Q. Z., Galvanetto, U., 2019. Static solution of crack propagation problems in peridynamics. Computer Methods in Applied Mechanics and Engineering 346, 126–151.

Nooru-Mohamed, M., Schlangen, E., van Mier, J. G., 1993. Experimental and numerical study on the behavior of concrete subjected to biaxial tension and shear. Advanced cement based materials 1 (1), 22–37.

Oliver, J., 1996. Modelling strong discontinuities in solid mechanics via strain softening constitutive equations, part 1: fundamentales. Internat. J. Numer. Methods Engrg. 39, 3575–3600.

Petersson, P.-E., 1981. Crack growth and development of fracture zones in plain concrete and similar materials.

Planas, J., Elices, M., Guinea, G., 1993. Cohesive cracks versus nonlocal models: Closing the gap. International Journal of Fracture 63 (2), 173–187.

Reinhardt, H. W., Cornelissen, H. A., Hordijk, D. A., 1986. Tensile tests and failure analysis of concrete. Journal of structural engineering 112 (11), 2462–2477.

Rots, J. G., 1988. Computational modeling of concrete fracture.

Shao, J. F., Rudnicki, J. W., 2000. A microcrack-based continuous damage model for brittle geomaterials. Mechanics of Materials 32 (10), 607–619.

Shojaei, A., Mudric, T., Zaccariotto, M., Galvanetto, U., 2016. A coupled meshless finite point/peridynamic method for 2d dynamic fracture analysis. International Journal of Mechanical Sciences 119, 419–431.

Silling, S. A., 2000. Reformulation of elasticity theory for discontinuities and long-range forces. Journal of the Mechanics and Physics of Solids 48 (1), 175–209.

Silling, S. A., Askari, E., 2005. A meshfree method based on the peridynamic model of solid mechanics. Computers & structures 83 (17-18), 1526–1535.

Silling, S. A., Epton, M., Weckner, O., Xu, J., Askari, E., 2007. Peridynamic states and constitutive modeling. Journal of Elasticity 88 (2), 151–184.

Silling, S. A., Lehoucq, R., 2010. Peridynamic theory of solid mechanics. In: Advances in applied mechanics. Vol. 44. Elsevier, pp. 73–168.

Stolarska, M., Chopp, D. L., Moës, N., Belytschko, T., 2001. Modelling crack growth by level sets in the extended finite element method. International journal for numerical methods in Engineering 51 (8), 943–960.

Tong, Y., Shen, W., Shao, J., Chen, J., 2020. A new bond model in peridynamics theory for progressive failure in cohesive brittle materials. Engineering Fracture Mechanics 223, 106767.

Trunk, B. G., 1999. Einfluss der bauteilgrösse auf die bruchenergie von beton. Ph.D. thesis, ETH Zurich.

Unger, J. F., Eckardt, S., Könke, C., 2007. Modelling of cohesive crack growth in concrete structures with the extended finite element method. Computer methods in applied mechanics and engineering 196 (41-44), 4087–4100.

Wang, Y., Han, F., Lubineau, G., 2019. A hybrid local/nonlocal continuum mechanics modeling and simulation of fractures in brittle materials. Computer Modeling in Engineering & Sciences 121 (2), 399–423.

Winkler, B., Hofstetter, G., Lehar, H., 2004. Application of a constitutive model for concrete to the analysis of a precast segmental tunnel lining. International Journal for Numerical and Analytical Methods in Geomechanics 28 (7-8), 797–819.

Winkler, B., Hofstetter, G., Niederwanger, G., 2001. Experimental verification of a constitutive model for concrete cracking. Proceedings of the Institution of Mechanical Engineers, Part L: Journal of Materials: Design and Applications 215 (2), 75–86.

Wu, J.-Y., 2017. A unified phase-field theory for the mechanics of damage and quasi-brittle failure. Journal of the Mechanics and Physics of Solids 103, 72–99.

Wu, J.-Y., Li, F.-B., Xu, S.-L., 2015. Extended embedded finite elements with continuous displacement jumps for the modeling of localized failure in solids. Computer Methods in Applied Mechanics and Engineering 285, 346–378.

Wu, J.-Y., Nguyen, V. P., Nguyen, C. T., Sutula, D., Bordas, S., Sinaie, S., 2018. Phase field modeling of fracture. Advances in Applied Mechancis: Multi-scale Theory and Computation 52.

Wu, J.-Y., Qiu, J.-F., Nguyen, V. P., Mandal, T. K., Zhuang, L.-J., 2019. Computational modeling of localized failure in solids: Xfem vs pf-czm. Computer Methods in Applied Mechanics and Engineering 345, 618–643.

Yang, D., Dong, W., Liu, X., Yi, S., He, X., 2018. Investigation on mode-i crack propagation in concrete using bond-based peridynamics with a new damage model. Engineering Fracture Mechanics 199, 567–581.

Zaccariotto, M., Mudric, T., Tomasi, D., Shojaei, A., Galvanetto, U., 2018. Coupling of fem meshes with peridynamic grids. Computer Methods in Applied Mechanics and Engineering 330, 471–497.

Zaccariotto, M., Tomasi, D., Galvanetto, U., 2017. An enhanced coupling of pd grids to fe meshes. Mechanics Research Communications 84, 125–135.

Zeng, Q.-D., Yao, J., Shao, J., 2018. Numerical study of hydraulic fracture propagation accounting for rock anisotropy. Journal of Petroleum Science and Engineering 160, 422–432.

554 Zeng, Q.-D., Yao, J., Shao, J., 2019. Study of hydraulic fracturing in an anisotropic poroelastic medium via a hybrid edfm-xfem
555 approach. Computers and Geotechnics 105, 51–68.
556 Zhang, H., Qiao, P., 2018. A state-based peridynamic model for quantitative fracture analysis. International Journal of Fracture
557 211 (1-2), 217–235.
558 Zhang, Y., Lackner, R., Zeiml, M., Mang, H. A., 2015. Strong discontinuity embedded approach with standard sos formulation:
559 Element formulation, energy-based crack-tracking strategy, and validations. Computer Methods in Applied Mechanics and
560 Engineering 287, 335–366.
561 Zhao, L.-Y., Shao, J.-F., Zhu, Q.-Z., 2018. Analysis of localized cracking in quasi-brittle materials with a micro-mechanics based
562 friction-damage approach. Journal of the Mechanics and Physics of Solids 119, 163–187.
563 Zhu, Q. Z., Ni, T., 2017. Peridynamic formulations enriched with bond rotation effects. International Journal of Engineering
564 Science 121, 118–129.
565 Zi, G., Bažant, Z. P., 2003. Eigenvalue method for computing size effect of cohesive cracks with residual stress, with application
566 to kink-bands in composites. International Journal of Engineering Science 41 (13-14), 1519–1534.
567 Zienkiewicz, O. C., Taylor, R. L., Nithiarasu, P., Zhu, J., 1977. The finite element method. Vol. 3. McGraw-hill London.